EXPLOSIVE WELDING, FORMING AND COMPACTION
Edited by T.Z. BLAZYNSKI, APPLIED SCIENCE PUBLISHERS, 1983

Chapter 2

PROPAGATION OF STRESS WAVES IN METALS

M. A. MEYERS

Department of Metallurgical and Materials Engineering,
New Mexico Institute of Mining and Technology,
Socorro, New Mexico, USA
and
L. E. MURR

Oregon Graduate Center,
Beaverton, Oregon, USA

2.1. DYNAMIC PROPAGATION OF DEFORMATION

The application of an external force to a body is, by definition a dynamic process. However, when the rate of change of the applied forces is low, one can consider the process of deformation as a sequence of steps in which the body can be considered in static equilibrium. Figure 2.1 shows how the distance between the atoms changes upon the application of an external force F. For each of the stages of deformation shown in Figs. 2.1(b) and 2.1(c), the body can be considered under static equilibrium and one can apply the methods of mechanics of materials to determine the internally-resisting stresses (by the method of sections). Hence, a section made at AA or BB will yield identical stresses.

However, the internal stresses are not instantaneously transmitted from the force-application region to the different regions of the body. The stresses (and strains) are transferred from atom to atom at a certain specific velocity. Figure 2.2(a) shows the application of a force at a rate dP/dt such that the stresses (and attendant strains) vary from section to section. Section BB has not 'seen' the application of the force at time t_1, while, at section AA, the separation between the atoms varies from point to point along the bar. One could establish a preliminary criterion for

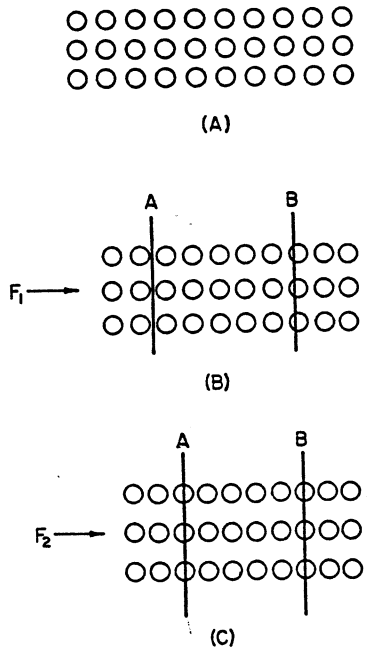

FIG. 2.1 Effect of application of force F on structure of solid (elastic deformation) under quasi-static conditions.

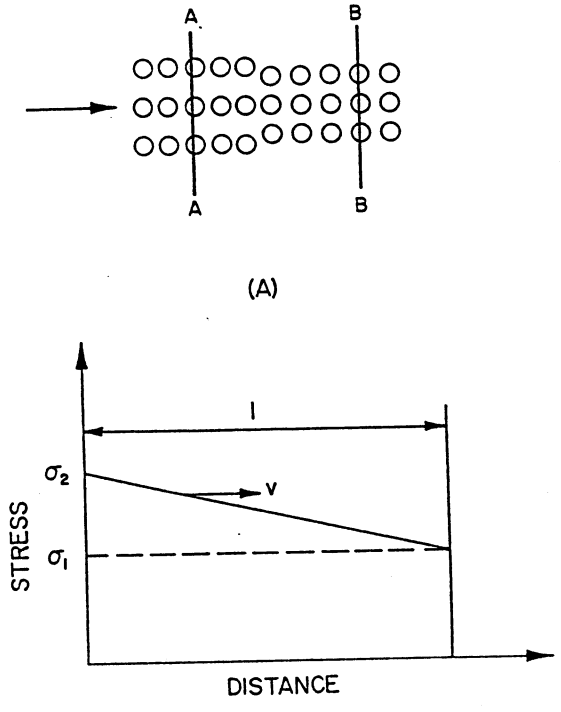

FIG. 2.2 (a) Wave propagation (elastic) in solid when rate of application of force is high. (b) Stress versus distance showing propagation of a general disturbance with velocity v.

'dynamic' deformation by stating that it requires a variation of stress (from one end to the other) of 10 per cent. If the velocity of the stress pulse is v and the length of the bar is l, one has, from Fig. 2.2(b):

$$\frac{\mathrm{d}\sigma}{\mathrm{d}t}=\frac{\sigma_2-\sigma_1}{t} \tag{2.1}$$

$$v=\frac{l}{t} \tag{2.2}$$

Equating t in eqns. (2.1) and (2.2):

$$\frac{\sigma_2-\sigma_1}{\left(\frac{\mathrm{d}\sigma}{\mathrm{d}t}\right)}=\frac{l}{v} \tag{2.3}$$

The criterion of 10 per cent variation in σ can be expressed as:

$$\sigma_2-\sigma_1\leqslant 0.1\sigma_{\max} \tag{2.4}$$

Substituting this into eqn. (2.3), one has:

$$\frac{\mathrm{d}\sigma}{\mathrm{d}t}\leqslant\frac{0.1v\sigma_{\max}}{l} \tag{2.5}$$

This is, of course, a somewhat arbitrary criterion, but it establishes the value of the rate of load application at which the 'dynamic' aspects or wave-propagation effects become important. In the wave-propagation regime, deformation is localized at the wavefront and release part and the behavior of the material is not only quantitatively but also qualitatively different.

At an atomic level, one may envisage the wave as a succession of impacts between adjacent atoms. Each atom, upon being accelerated to a certain velocity, transmits its (or part of) momentum to its neighbor(s).

The mass, separation between, and forces of attraction and repulsion of atoms determine the way in which the stress pulse is carried from one point to the other. Of importance also is the stress state established by the pulse, which determines the relative direction of motion of atoms and stress pulse, and the extent of motion of atoms. As a result of these differences, one can classify the stress pulses into three categories: (a) elastic, (b) plastic and (c) shock waves. Elastic waves produce only elastic deformation in the material. On an atomic scale, all atoms return to the original position in relation to their neighbors. There are two classes of

elastic waves: longitudinal (or irrotational, dilatational, *P*) and shear (or equivoluminal, transverse, distortional, *S*) waves. They travel at velocities that are determined by their elastic constants. One may add a third class of elastic wave to the two above: surface, Love, or Raleigh waves, which travel at the surface. These are the commonly known waves propagating in water. Elastic waves are treated in Section 2.2. When the amplitude of the elastic wave exceeds a critical value for the yield stress of the material, at that specific strain rate (and we know that the yield stress of most metals is strain-rate dependent) the atoms undergo permanent changes in position with respect to their neighbors: macroscopically, this entails a change in the dimensions of the body. These are called plastic (or elastoplastic) waves. Depending upon their nature, one may also have plastic longitudinal or shear waves. These waves are treated in Section 2.3. If the geometry of the body is such that it allows a strain state called 'uniaxial strain', the propagation velocity of the plastic wave increases with increasing pressure because there cannot be any lateral flow of material (perpendicular to the direction of propagation of the waves). The wave takes the configuration shown in Fig. 2.3(b): the sharp front is

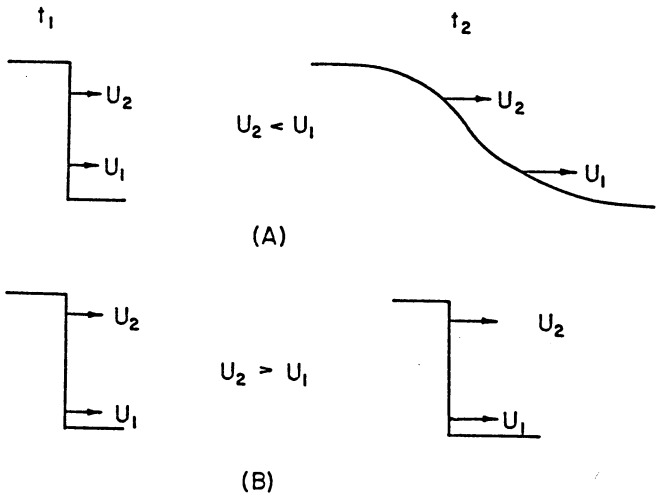

FIG. 2.3 Propagation of disturbances. (a) When $U_2 < U_1$ disturbance front slope decreases with propagation distance. (b) When $U_2 > U_1$ 'shock' front forms and remains stable.

the characteristic that defines a shock wave. The shock waves are treated in Section 2.4. The most simplified treatment (hydrodynamic theory) is introduced first; then, some more contemporary considerations and techniques such as attenuation of shock waves, method of characteristics,

computer codes (incorporating the von Neumann-Richtmyer artificial viscosity) are discussed (Section 2.5). The fundamental aspects of the metallurgical effects of shock waves are discussed in Section 2.6. The specific residual microstructural and mechanical effects of a number of metals are treated in Chapter 3.

The treatment of this chapter will be kept at a level consistent with the 'engineering' approach of this book. There have been significant advances in the theoretical treatment of disturbances in solids in the past twenty years; these treatments, incorporated into computer programs, have dramatically increased the predictive capability. In-depth studies of disturbances in solids are numerous and the reader is referred to references 1 to 21, and 25 to 31.

2.2. ELASTIC WAVES

2.2.1. Introduction

Three types of elastic waves can propagate in solids: longitudinal (or dilatational) waves, distortional (or equivoluminal) waves and surface (or Raleigh) waves. A brief concept of these waves is given below.

(*a*) *Longitudinal or dilatational waves.* In longitudinal waves, the particle and wave velocity have the same direction. If the wave is compressive, they have the same sense; if it is tensile, they have the opposite senses.

(*b*) *Distortional or equivoluminal waves.* In this case the displacement of the 'particles' and wave are perpendicular. There should be no change in density and all longitudinal strains ε_{11}, ε_{22}, ε_{33} are zero.

(*c*) *Surface waves.* The most obvious example of this type of wave are the waves in the sea. They only happen at interfaces. This type of wave is restricted to the region adjacent to the interface, and 'particle' velocity decreases very rapidly (exponentially) as one moves away from it. The particles describe elliptical trajectories. The Raleigh wave is the slowest of the three waves; the fastest is the longitudinal wave as will be seen from the derivations that follow. When the elastic limit (or the critical shear stress for plastic flow on the plane with highest Schmid factor) is reached, the elastic wave is followed by either a plastic or a plastic shock wave, depending on the state of stress (uniaxial stress and uniaxial strain, respectively.).

2.2.2. Elastic Waves in Isotropic Materials

Figure 2.4 shows a unit cube which is not in equilibrium. Consequently, the stresses acting on opposite faces are not identical. Newton's second law can be expressed, in relation to the three axes, as:

$$\begin{aligned} \sum Fx_1 &= \max_1, \\ \sum Fx_2 &= \max_2, \\ \sum Fx_3 &= \max_3, \end{aligned} \tag{2.6}$$

All stresses acting in the direction $0x_1$ are represented in the cube. It is considered that at the center of the cube (with dimensions δx_1, δx_2, δx_3) the stresses have the values of σ_{11}, σ_{22}, σ_{33} (normal) and σ_{12}, σ_{13}, σ_{23} (shear). In the derivations that follow the symbols defined by Nye[144] will be used.

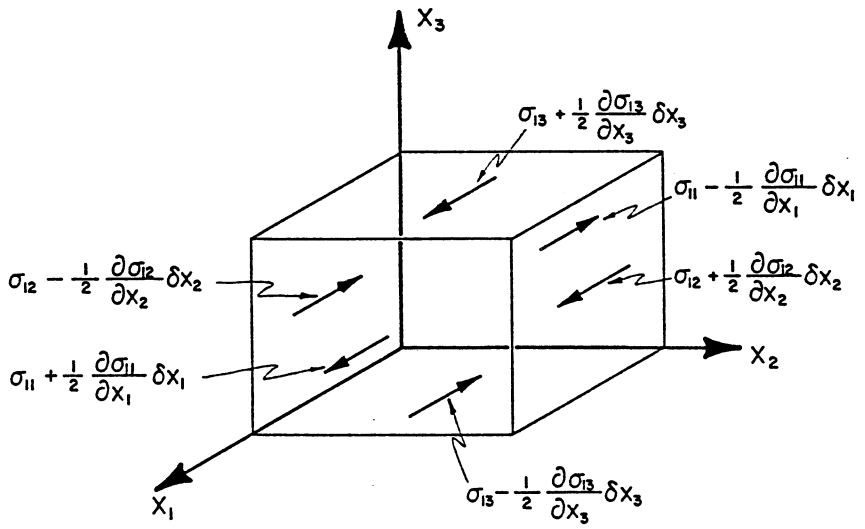

FIG. 2.4 Unit cube when stresses vary from one face to the other; only stresses in $0x_1$ direction shown.

The term $\frac{1}{2}(\partial\sigma_{11}/\partial x_1)\delta x_1$ expresses the change in σ_{11}, with respect to $0x_1$, as one moves from the center of the cube to one of the faces perpendicular to $0x_1$. The other terms have similar meanings. So, neglecting the effects of gravitational forces and body moments, one has, in the direction $0x_1$:

$$\left(\sigma_{11}+\frac{1}{2}\frac{\partial\sigma_{11}}{\partial x_1}\delta x_1-\sigma_{11}+\frac{1}{2}\frac{\partial\sigma_{11}}{\partial x_1}\delta x_1\right)\delta x_2\,\delta x_3$$

$$+\left(\sigma_{12}+\frac{1}{2}\frac{\partial\sigma_{12}}{\partial x_2}\delta x_2-\sigma_{12}+\frac{1}{2}\frac{\partial\sigma_{12}}{\partial x_2}\delta x_2\right)\delta x_1\,\delta x_3$$

$$+\left(\sigma_{13}+\frac{1}{2}\frac{\partial\sigma_{13}}{\partial x_3}\delta x_3-\sigma_{13}+\frac{1}{2}\frac{\partial\sigma_{13}}{\partial x_3}\delta x_3\right)\delta x_1\,\delta x_2$$

$$=\rho\delta x_1\delta x_2\delta x_3\frac{\partial^2 u_1}{\partial t^2}$$

u_i is the displacement in the direction x_i. The derivations that follow are based on Kolsky's[1] and Rinehart's[2] presentations. A similar account is given by Wasley.[10] So:

$$\frac{\partial\sigma_{11}}{\partial x_1}\delta x_1\,\delta x_2\,\delta x_3+\frac{\partial\sigma_{12}}{\partial x_2}\delta x_1\,\delta x_2\,\delta x_3+\frac{\partial\sigma_{13}}{\partial x_3}\delta x_1\,\delta x_2\,\delta x_3$$

$$=\rho\delta x_1\,\delta x_2\,\delta x_3\frac{\partial^2 x_1}{\partial t^2}$$

For the other eqns. (2.6):

$$\frac{\partial\sigma_{11}}{\partial x_1}+\frac{\partial\sigma_{12}}{\partial x_2}+\frac{\partial\sigma_{13}}{\partial x_3}=\rho\frac{\partial^2 u_1}{\partial t^2};$$

$$\frac{\partial\sigma_{21}}{\partial x_1}+\frac{\partial\sigma_{22}}{\partial x_2}+\frac{\partial\sigma_{23}}{\partial x_3}=\rho\frac{\partial^2 u_2}{\partial t^2};$$

$$\frac{\partial\sigma_{31}}{\partial x_1}+\frac{\partial\sigma_{32}}{\partial x_2}+\frac{\partial\sigma_{33}}{\partial x_3}=\rho\frac{\partial^2 u_3}{\partial t^2};$$

In dummy suffix notation

$$\frac{\partial\sigma_{ij}}{\partial x_j}=\rho\frac{\partial^2 u_i}{\partial t^2} \tag{2.7}$$

The solution of this system of differential equations will yield, once the stresses are replaced by strains, the equations of the wave. For an isotropic material, the calculations are simplified. There are only two independent elastic constants instead of 36. One has, for an isotropic

material:

$$\begin{aligned} &C_{12}=C_{13}=C_{23}=\lambda \\ &C_{44}=C_{55}=C_{66}=\mu \\ &C_{11}=C_{22}=C_{33}=\lambda+2\mu \\ &C_{14}=C_{15}=C_{16}=C_{24}=C_{25}=C_{26}=C_{34}=C_{35}=C_{36} \\ &\quad =C_{45}=C_{46}=C_{56}=0 \end{aligned} \tag{2.8}$$

Notice that the stiffnesses are represented by their matrix notation and *not* by their tensor notation. So:

$$\begin{aligned} &\sigma_{11}=\lambda\Delta+2\mu\varepsilon_{11}, \qquad \sigma_{23}=2\mu\varepsilon_{23}, \qquad \sigma_{22}=\lambda\Delta+2\mu\varepsilon_{22}, \\ &\sigma_{13}=2\mu\varepsilon_{13}, \qquad \sigma_{12}=2\mu\varepsilon_{12}, \qquad \sigma_{33}=\lambda\Delta+2\mu\varepsilon_{33} \end{aligned} \tag{2.9}$$

λ and μ are Lamé's constants and Δ is the dilatation: $\Delta=\varepsilon_{11}+\varepsilon_{22}+\varepsilon_{33}$ Replacing the values of σ_{ij} in eqns. (2.6) by their values in eqn. (2.9).

$$\frac{\partial}{\partial x_1}(\lambda\Delta+2\mu\varepsilon_{11})+\frac{\partial}{\partial x_2}(2\mu\varepsilon_{12})+\frac{\partial}{\partial x_3}(2\mu\varepsilon_{13})=\rho\frac{\partial^2 u_1}{\partial t^2}$$

$$2\mu\frac{\partial\varepsilon_{11}}{\partial x_1}+\mu\frac{\partial\varepsilon_{12}}{\partial x_2}+\mu\frac{\partial\varepsilon_{13}}{\partial x_3}=\rho\frac{\partial^2 u_1}{\partial t^2}$$

But, from the definition of strains, one has:

$$\varepsilon_{11}=\frac{\partial u_1}{\partial x_1}; \qquad \varepsilon_{12}=\frac{1}{2}\left(\frac{\partial u_1}{\partial x_2}+\frac{\partial u_2}{\partial x_1}\right) \quad \text{and} \quad \varepsilon_{13}=\frac{1}{2}\left(\frac{\partial u_1}{\partial x_3}+\frac{\partial u_3}{\partial x_1}\right)$$

So

$$2\mu\frac{\partial^2 u_1}{\partial x_1^2}+\mu\frac{\partial^2 u_1}{\partial x_2^2}+\mu\frac{\partial^2 u_2}{\partial x_1\partial x_2}+\mu\frac{\partial^2 u_1}{\partial x_3^2}+\mu\frac{\partial^2 u_3}{\partial x_1\partial x_3}+\frac{\partial\lambda\Delta}{\partial x_1}=\rho\frac{\partial^2 u_1}{\partial t^2}$$

We will define the operator ∇^2 as:

$$\nabla^2=\frac{\partial^2}{\partial x_1^2}+\frac{\partial^2}{\partial x_2^2}+\frac{\partial^2}{\partial x_3^2} \tag{2.10}$$

So

$$\lambda\frac{\partial\Delta}{\partial x_1}+\Delta\frac{\partial\lambda}{\partial x_1}+\mu\frac{\partial^2 u_1}{\partial x_1^2}+\mu\nabla^2 u_1+\mu\frac{\partial^2 u_2}{\partial x_1\partial x_2}+\mu\frac{\partial^2 u_3}{\partial x_1\partial x_3}=\frac{\partial^2 u_1}{\partial t^2}$$

and

$$(\lambda+\mu)\frac{\partial\Delta}{\partial x_1}+\mu\nabla^2 u_1=\rho\frac{\partial^2 u_1}{\partial t^2} \tag{2.11}$$

Repeating the procedure for the other two eqns. (2.6):

$$(\lambda+\mu)\frac{\partial\Delta}{\partial x_2}+\mu\nabla^2 u_2=\rho\frac{\partial^2 u_2}{\partial t^2} \tag{2.12}$$

$$(\lambda+\mu)\frac{\partial\Delta}{\partial x_3}+\mu\nabla^2 u_3=\rho\frac{\partial^2 u_3}{\partial t^2} \tag{2.13}$$

Still, the displacements have to be replaced by strains and the three equations have to be grouped into one. For this, we take the derivative with respect to x_1 of eqn. (2.11), with respect to x_2 of eqn. (2.12), and with respect to x_3 of eqn. (2.13).

$$\begin{aligned}(\lambda+\mu)\frac{\partial^2\Delta}{\partial x_1^2}+\mu\frac{\partial}{\partial x_1}\nabla^2 u_1&=\rho\frac{\partial^3 u_1}{\partial t^2\partial x_1}\\ (\lambda+\mu)\frac{\partial^2\Delta}{\partial x_1^2}+\mu\nabla^2\frac{\partial u_1}{\partial x_1}&=\rho\frac{\partial^2\varepsilon_{11}}{\partial t^2}\\ (\lambda+\mu)\frac{\partial^2\Delta}{\partial x_1^2}+\mu\nabla^2\varepsilon_{11}&=\rho\frac{\partial^2\varepsilon_{11}}{\partial t^2}\end{aligned} \tag{2.14}$$

Repeating the procedure for eqns. (2.12) and (2.13):

$$(\lambda+\mu)\frac{\partial^2\Delta}{\partial x_2^2}+\mu\nabla^2\varepsilon_{22}=\rho\frac{\partial^2\varepsilon_{22}}{\partial t^2} \tag{2.15}$$

$$(\lambda+\mu)\frac{\partial^2\Delta}{\partial x_3^2}+\mu\nabla^2\varepsilon_{33}=\rho\frac{\partial^2\varepsilon_{33}}{\partial t^2} \tag{2.16}$$

Adding eqns. (2.14), (2.15) and (2.16):

$$(\lambda+\mu)\nabla^2\Delta+\mu\nabla^2(\varepsilon_{11}+\varepsilon_{22}+\varepsilon_{33})=\rho\frac{\partial}{\partial t^2}(\varepsilon_{11}+\varepsilon_{22}+\varepsilon_{33})$$

and

$$(\lambda+2\mu)\nabla^2\Delta=\rho\frac{\partial^2\Delta}{\partial t^2}$$

or

$$\frac{\partial^2\Delta}{\partial t^2}=\left(\frac{\lambda+2\mu}{\rho}\right)\nabla^2\Delta \tag{2.17}$$

A dimensional analysis shows that the units of the coefficient $(\lambda+2\mu)/\rho$ are (distance/time)^2. A closer comparison with equations of waves given in

basic textbooks shows that:

$$V_{\text{long}} = \left(\frac{\lambda+2\mu}{\rho}\right)^{1/2} \tag{2.18}$$

If one assumes that $\nu=0.3$, one obtains

$$V_{\text{long}}=\left(\frac{1.35E}{\rho}\right)^{1/2}$$

Indeed, Kreyzig[22] has obtained the following equations for one-dimensional (vibrating string) and two-dimensional waves:

$$\frac{\partial^2 u_1}{\partial t^2}=C^2\frac{\partial^2 u_1}{\partial x_1^2} \qquad \text{(for 1-D wave)} \tag{2.19}$$

$$\frac{\partial^2 u}{\partial t^2}=C^2\nabla^2 u$$

The elimination of Δ between eqns. (2.11) and (2.12) yields the shear wave. For this, we differentiate eqn. (2.11) with respect to x_2 and eqn. (2.12) with respect to x_1:
From eqn. (2.11)

$$(\lambda+\mu)\frac{\partial^2\Delta}{\partial x_1\partial x_2}+\mu\frac{\partial}{\partial x_2}\nabla^2 u_1=\rho\frac{\partial^3 u_1}{\partial x_2\partial t^2} \tag{2.20}$$

From eqn. (2.12)

$$(\lambda+\mu)\frac{\partial^2\Delta}{\partial x_2\partial x_1}+\mu\frac{\partial}{\partial x_1}\nabla^2 u_2=\rho\frac{\partial^3 u_2}{\partial x_1\partial t^2} \tag{2.21}$$

$$\rho\frac{\partial^2}{\partial t^2}\left(\frac{\partial u_1}{\partial x_2}-\frac{\partial u_2}{\partial x_1}\right)=\mu\nabla^2\left(\frac{\partial u_1}{\partial x_2}-\frac{\partial u_2}{\partial x_1}\right) \tag{2.22}$$

But, by definition, the rigid body rotations are given by:

$$\omega_{ij}=\frac{1}{2}\left(\frac{\partial u_i}{\partial x_j}-\frac{\partial u_j}{\partial x_i}\right) \tag{2.23}$$

And hence,

$$\frac{\partial^2\omega_{12}}{\partial t^2}=\frac{\mu}{\rho}\nabla^2\frac{\partial\omega_{12}}{\partial x_i} \tag{2.24}$$

Thus, the rotation ω_{12} propagates at the velocity $(\mu/\rho)^{1/2}$. The same procedure can be repeated to obtain rotations ω_{13} and ω_{23}.

$$V_{\text{shear}} = (\mu/\rho)^{1/2} \tag{2.25}$$

For the treatment of the surface waves the reader is referred to Kolsky.[1] For steel ($\nu = 0.29$) a calculation reported by Kolsky[1] shows the velocity is:

$$V_{\text{Raleigh}} = 0.9258\ V_{\text{shear}}$$

Typical velocities of longitudinal and shear waves are reported in Table 2.1.

TABLE 2.1
VELOCITIES OF ELASTIC WAVES

Material	V_{long}(*m/sec*)	V_{shear}(*m/sec*)
Air	340	None
Aluminum	6 100	3 100
Steel	5 800	3 100
Lead	2 200	700

2.2.3. Elastic Waves in Anisotropic Media

In anisotropic media the situation complicates itself. Because deformation mechanisms operate on a microscopic scale, and because metals are, on a microscopic scale, anisotropic, wave anisotropy should be understood. The derivation of wave velocities for crystals exhibiting cubic symmetry is presented by Ghatak and Kothari[3] and is summarized here.

When eqn. (2.7) is substituted into eqns. (2.4), the stiffnesses of cubic symmetry have to be used. In a cubic crystal, there are three independent elastic constants: C_{11}, C_{12} and C_{44}.

So

$$\begin{aligned}
\sigma_1 &= (C_{11} - C_{12})\varepsilon_1 + C_{12}(\varepsilon_1 + \varepsilon_1 + \varepsilon_3) \\
\sigma_2 &= (C_{11} - C_{12})\varepsilon_2 + C_{12}(\varepsilon_1 + \varepsilon_2 + \varepsilon_3) \\
\sigma_3 &= (C_{11} - C_{12})\varepsilon_3 + C_{12}(\varepsilon_1 + \varepsilon_3 + \varepsilon_3) \\
\sigma_4 &= C_{44}\varepsilon_4 \\
\sigma_5 &= C_{44}\varepsilon_5 \\
\sigma_6 &= C_{44}\varepsilon_6
\end{aligned} \tag{2.26}$$

We should remember that

$$\varepsilon_m = 2\varepsilon_{ij} = \left(\frac{\partial u_i}{\partial x_j} + \frac{\partial u_j}{\partial x_i}\right) \tag{2.27}$$

So, we have

$$(C_{11}-C_{12})\frac{\partial^2 u_1}{\partial x_1^2} + C_{12}\left(\frac{\partial^2 u_1}{\partial x_1^2} + \frac{\partial^2 u_2}{\partial x_1 \partial x_2} + \frac{\partial^2 u_3}{\partial x_1 + \partial x_3}\right)$$
$$+ C_{44}\left(\frac{\partial^2 u_1}{\partial x_2^2} + \frac{\partial^2 u_1}{\partial x_3^2} + \frac{\partial^2 u^2}{\partial x_1 \partial x_2} + \frac{\partial^2 u_3}{\partial x_1 \partial x_3}\right) = \rho \frac{\partial^2 u_1}{\partial t^2} \tag{2.28}$$

and two other, similar equations.

We now have to group these three equations into one, and at the same time eliminate the displacements u_i. By making the following substitution:

$$u_i = A_i \exp(-ij(\omega t - \mathbf{q}\cdot\mathbf{v})) \tag{2.29}$$

we are assuming that we have a plane wave with angular frequency ω; the wave vector is $\mathbf{q}$·ij should not be confused with i. ij is the imaginary number. We end up with a set of three homogeneous equations, whose solutions are given by the secular equation or determinant below.

$$\begin{bmatrix} (C_{11}-C_{44})q_1^2 + C_{44}q^2 - \rho\omega^2 & (C_{12}+C_{44})q_1q_2 & (C_{12}+C_{44})q_1q_3 \\ (C_{12}+C_{44})q_2q_1 & (C_{11}-C_{44})q_2^2 + C_{44}q^2 - \rho\omega^2 & (C_{12}+C_{44})q_2q_3 \\ (C_{12}+C_{44})q_3q_1 & (C_{12}+C_{44})q_2q_3 & (C_{11}-C_{44})q_3^2 + C_{44}q^2 - \rho\omega^2 \end{bmatrix} \tag{2.30}$$

We have $q^2 = q_1^2 + q_2^2 + q_3^2$

We can determine the solution of this equation for certain orientations of the wave, e.g.

(*a*) [100] $q_1 = q$, $q_2 = 0 = q_3$

$$(C_{11}q^2 - \rho\omega^2)(C_{44}q^2 - \rho\omega^2)^2 = 0, \qquad C_{11}q^2 - \rho\omega^2 = 0,$$

and

$$C_{44}q^2 - \rho\omega^2 = 0 \tag{2.31}$$

The following are solutions:

$$U_1 = \frac{\omega}{q} = (C_{11}/\rho)^{1/2}, \quad \text{and} \quad U_2 = U_3 = (C_{44}/\rho)^{1/2} \tag{2.32}$$

The ratio ω/q is the velocity of the wave. (See eqns. (2.34) in ref. 3) U_1 is the longitudinal wave; U_2 and U_3 are the shear waves.

(*b*) [110] For this orientation of **q**, we have $q_1 = q_2 = q/\sqrt{3}$; $q_3 = 0$. The secular equation becomes:

$$(C_{44}q^2 - \rho\omega^2)\left[(\tfrac{1}{2}C_{11}q^2 + C_{44}q^2 - \rho\omega^2)(\tfrac{1}{2}C_{11}q^2 + C_{44}q^2 - \rho\omega^2) - (C_{11} + C_{44})(C_{12} + C_{44})\frac{q^4}{4}\right] = 0 \quad (2.33)$$

This equation accepts the following solutions:

$$C_{44}q^2 - \rho\omega^2 = 0, \qquad U_3 = (C_{44}/\rho)^{1/2} \quad (2.34)$$

$$(\tfrac{1}{2}C_{11}q^2 + C_{44}q^2 - \rho\omega^2)^2 - (C_{11} + C_{44})(C_{12} + C_{44})\frac{q^4}{4} = 0$$

$$\tfrac{1}{4}C_{11}^2q^4 + C_{44}^2q^4 - \rho^2\omega^4 + C_{11}C_{44}q^4 - C_{11}\rho\omega^2q^2 - 2C_{44}\rho\omega^2q^2 - (C_{11} + C_{44})(C_{12} + C_{44})\frac{q^4}{4} = 0 \quad (2.35)$$

Dividing by q^4 the two solutions are:

$$U_1 = \left(\frac{C_{11} + C_{12} + 2C_{44}}{2\rho}\right)^{1/2}, \quad \text{and} \quad U_2 = \left(\frac{C_{11} - C_{12}}{2\rho}\right)^{1/2} \quad (2.36)$$

Where U_1 is the longitudinal wave, U_2 is the shear wave with vibration along the x_1, x_2 axes, and U_3 the shear wave with vibration along the x_3 axis.

(*c*) [111]
We find that

$$U_1 = \left(\frac{2C_{11} + C_{12} + 2C_{44}}{3\rho}\right)^{1/2},$$

and,

$$U_2 = U_3 = \left(\frac{C_{11} - C_{12} + C_{44}}{3\rho}\right)^{1/2} \quad (2.37)$$

It is interesting to observe that, if a material is isotropic, the velocities of the waves reduce themselves to the ones calculated for isotropic materials. An isotropic material has the anisotropy ratio equal to 1

$$A = 1 = \frac{2C_{44}}{C_{11} - C_{12}}$$

therefore

$$C_{44}=\frac{C_{11}-C_{12}}{2}$$

Substituting this into eqns. (2.32), (2.34), (2.36) and (2.37), one obtains:

$$U_1[100]=U_1[110]=U_1[111]=(C_{11}/\rho)^{1/2} \tag{2.38}$$

$$U_2[100]=U_3[100]=U_2[110]=U_3[110]$$
$$=U_2[111]=U_3[111]=(C_{44}/\rho)^{1/2} \tag{2.39}$$

Lamé's constants have the following values:

$$C_{44}=\mu, \qquad C_{12}=\lambda \tag{2.40}$$

So $C_{11}=2C_{44}+C_{12}=2\mu+\lambda$. Consequently, eqns. (2.38) and (2.39) reduce themselves to:

$$U_1=\left(\frac{2\mu+\lambda}{\rho}\right)^{1/2}, \qquad U_2=\left(\frac{\mu}{\rho}\right)^{1/2} \tag{2.41}$$

These are, in fact, eqns. (2.18) and (2.25).

An idea of the dependence of elastic wave velocity upon orientation for an FCC metal can be obtained from the calculations performed by Meyers and Carvalho.[23]

For Ni, at ambient temperature (ref. 3): ($\rho=8.9$)

$$C_{11}=2.508\times10^{11}\text{ Pa}, \quad C_{12}=1.500\times10^{11}\text{ Pa}, \quad C_{44}=1.235\times10^{11}\text{ Pa}$$

Hence

$$U_{[100]}=5.31\times10^3\text{ m/sec}, \qquad U_{[110]}=6.03\times10^3\text{ m/sec},$$
$$U_{[111]}=5.80\times10^3\text{ m/sec}$$

2.3. PLASTIC WAVES

2.3.1. Preliminary Considerations

Every plastic deformation propagates within a solid as a disturbance in the same way as elastic deformation. However, when the rate of application of the load is low with respect to the velocity of propagation of the disturbance, one can consider the plastic strain as uniformly distributed over the whole extent of the solid body (at the macroscopic level,

because microscopically plastic deformation is inherently inhomogeneous). The velocity is given by:

$$v \sim \left(\frac{d\sigma}{dt}\right)^{1/2} \tag{2.42}$$

The work hardening rate is lower than Young's modulus. For the uniaxial stress configuration, $d\sigma/d\varepsilon$ decreases with ε. This, in turn will produce a plastic wave whose velocity decreases with strain. Hence, the wave front will have a lower and lower slope as it propagates through the metal (Fig. 2.3(a)). If no lateral flow of material is allowed (flow perpendicular to the direction of propagation of the wave), the stress–strain curve takes a concave appearance (in contrast to a convex shape for uniaxial, biaxial, and similar stress states). The Hugoniot pressure versus volume curve can be converted into a stress versus strain curve (Fig. 2.8(b)) where the increase in slope with strain can be seen. This configuration defines the shock wave, which will be treated separately in Section 4. It is seen that between the state of uniaxial stress established in a thin wire and the state of uniaxial strain set up in an infinite (laterally) plate, one has a whole spectrum of stress regimes, leading from a gently sloping stress front to a discontinuous shock front. In the former case the hydrostatic component of the stress is zero; in the latter, it is very high (as high as allowed by the uniaxial strain).

Although one can consider the plastic waves to be of a pure shock nature in carefully controlled shock-loading experiments, explosive forming, welding and compaction present a mixture of these waves. In explosive forming, one has plastic waves propagating *along* the sheet; shock waves could only exist while passing through it. Nevertheless, this would require simultaneous arrival of the shock front over the whole surface of the sheet, which is not the case. In shock-wave compaction, one can distinguish two regions: (a) the core of the particles, which do not undergo any macroscopic deformation and are consequently subjected to a shock wave, and (b) the particle periphery, which is formed in such a way as to fill the gaps between particles. Figure 2.5 shows how a shock front compacts initially spherical particles. There has to be a continual (plastic wave)⇆(shock wave) conversion as the wave travels through the system. The regions undergoing residual plastic deformation are responsible for a dispersion of the wave. Additional complications are the friction between particles. The increased attenuation rate of the plastic wave (resulting in increased heating) contributes significantly to the interparticle bonding. Melting often occurs at the interfaces.

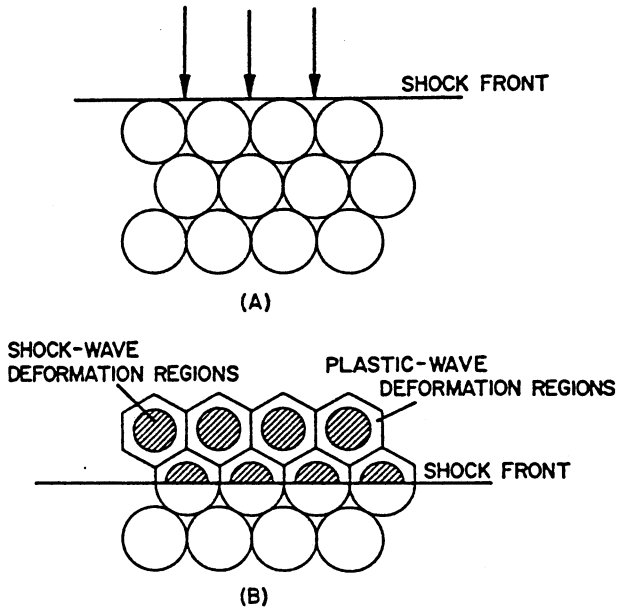

FIG. 2.5 Propagation of disturbance in metal powder producing consolidation. Only the internal portion of particle undergoes a shock deformation. External portions suffer heavy residual deformation and are traversed by plastic waves.

2.3.2. The von Kármán and Duwez Plastic Wave Theory

Von Kármán and Duwez,[5] G. I. Taylor[32] and Rakhmatulin[33] independently developed the theory of plastic waves. The von Kármán and Duwez treatment is presented here. Two frames of reference used when dealing with disturbance-propagation problems are: (a) Lagrangian, when one considers a particle in the material and observes the change of position of this particle with time; and (b) Eulerian, when one considers a certain region in space and observes the flow of material in and out of it. Hence, a property F, which varies with time, spatial position (X) and particle position (x), can either be expressed as:

$$F=f(x,t), \quad \text{or} \quad F=f(X,t) \tag{2.43}$$

These two approaches will be discussed again in Section 2.5, in connection with numerical methods of solution.

Von Kármán and Duwez considered the simplest possible plastic wave propagation problem: a semi-infinite thin wire being impacted at a certain velocity generating a downward motion at a velocity V_1. The initial position of the extremity of the wire is taken as the origin, and we observe the displacement of a particle situated at the position x. At time

t, it will be displaced by u. Hence

$$dF = dm\frac{\partial^2 u}{\partial t^2} = \rho_0 A_0\, dx\frac{\partial^2 u}{\partial t^2}$$

therefore

$$\frac{d\sigma}{dx} = \rho_0\frac{\partial^2 u}{\partial t^2} \tag{2.44}$$

where ρ_0 and A_0 are the initial density and area, and σ is the stress. Since we have a state of plastic deformation, and assuming that one has a univalent relationship between stress and strain in *loading* (not in unloading because of the irreversibility of the process), one can write,

$$\rho_0\frac{\partial^2 u}{\partial t^2} = \frac{d\sigma}{d\varepsilon}\frac{\partial \varepsilon}{\partial x}$$

and with $\varepsilon = \partial u/\partial x$, we have

$$\frac{\partial^2 u}{\partial t^2} = \frac{1}{\rho_0}\frac{d\sigma}{d\varepsilon}\frac{\partial^2 u}{\partial x^2} \tag{2.45}$$

One can see the similarity with eqn. (2.19). The velocity of the plastic wave can be seen to be given by

$$\left(\frac{1}{\rho_0}\frac{d\sigma}{d\varepsilon}\right)^{1/2}$$

and the comparable elastic wave velocity can also be determined.[34,35]

The application of the boundary conditions allows the determination of the wave profile. The boundary conditions are

$$u = V_1 t \text{ at } x_1 = 0, \quad \text{and} \quad u = 0 \text{ at } x = \infty \qquad (\text{any } t > 0)$$

There are two solutions to eqn. 2.45. The first (found by inspection) is

$$u = V_1 t + \varepsilon_1 x$$

A second solution is found when

$$\frac{\left(\frac{d\sigma}{d\varepsilon}\right)}{\rho_0} = \left(\frac{x}{t}\right)^2$$

$d\sigma/d\varepsilon$ being a function of ε, the strain ε has to be a function of the

velocity x/t, which we will call β

$$u=\int_{\infty}^{x}\frac{\partial u}{\partial x}\,dx=\int_{\infty}^{x}f(\beta)\,dx=t\int_{-\infty}^{\beta}f(\beta)\,d\beta \tag{2.46}$$

Differentiating twice with respect to t, we get:

$$\frac{\partial^2 u}{\partial t^2}=\frac{\beta^2}{t}f'(\beta) \tag{2.47}$$

where $f'(\beta)$ is the derivative of $f(\beta)$ with respect to β. This leads to the following solution:

(a) $x=0$ to $x=Ct$ (C is the velocity of propagation of the plastic wavefront); the strain is constant at ε_1.

(b) $Ct<x<C_0t$ (C_0 is the velocity of elastic longitudinal waves in bars). In this interval, one has:

$$\frac{x}{t}=\left(\frac{d\sigma/d\varepsilon}{\rho_0}\right)^{1/2} \tag{2.48}$$

(c) $x>C_0t$, $\varepsilon=0$.

Figure 2.6 shows graphically how the strain varies as a function of x/t.

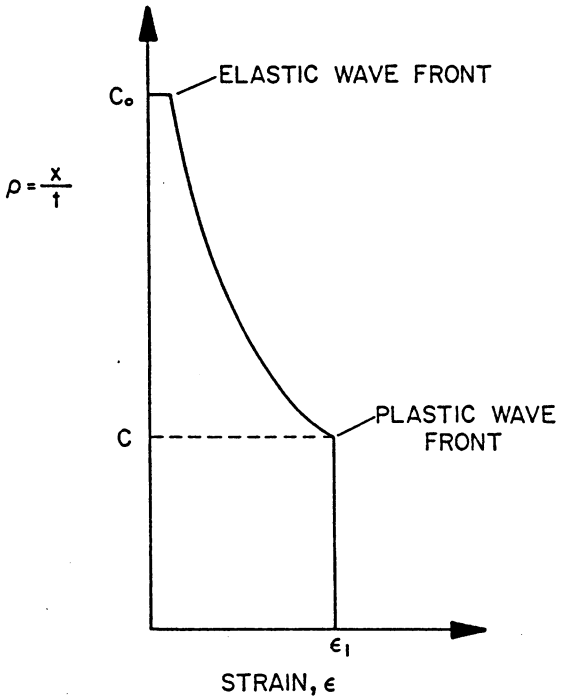

FIG. 2.6 Strain versus x/t for disturbance propagating in wire (adapted from von Kármán and Duwez[5])

From eqn. (2.46) for $u(0,t)=V_1 t$, we have

$$V_1 = -\int_0^{\varepsilon_1} \left(\frac{d\sigma/d\varepsilon}{\rho_0}\right)^{1/2} d\varepsilon \tag{2.49}$$

For a known impact velocity and a known σ versus ε relationship, one can determine ε. Assuming a power law:

$$\sigma = k\varepsilon^n, \qquad V_1 = -\frac{k\varepsilon_1^n}{\rho_0} \tag{2.50}$$

and

$$\varepsilon_1 = \left(\frac{\rho_0 V_1}{k}\right)^{1/n} \tag{2.51}$$

The maximum impact velocity can be easily found by setting it equal to the velocity that will produce necking on the specimen. Applying Considère's criterion $\varepsilon = n$,

$$V_1 = -(kn^n/\rho_0) \tag{2.52}$$

2.3.3. Plastic Shear Waves

One can have plastic shear waves, in an analogous way to elastic shear waves. The particles undergo plastic displacement perpendicular to the direction of propagation of the wave. It is very difficult to generate exclusively plastic shear waves, and a wave in a rod would be a plastic shear wave; however, the amplitude of motion would vary with the distance from the longitudinal axis of the rod. Hence, it is easier to generate a plastic shear wave simultaneously with a longitudinal stress wave. For the mathematical treatment of plastic shear waves see references 32, 36 and 37. However, it is Clifton's group[25-27,39] that has investigated them—both experimentally and theoretically—in greater depth. Using a parallel inclined impact of a projectile with a target, it is seen that the impact generates a pressure wave moving perpendicular to the interface and a shear wave, producing lateral displacement, also moving perpendicular to it. Measurement of the lateral displacement determines the rate of arrival of this shear disturbance at the back face of the target. Figure 2.7 shows the transverse displacement as a function of time after impact for 6061-T6 aluminum. It can be seen that the slope of the line is constant over the interval. Hence, the shear wave differs from a shock wave in the gradually increasing front. For the situation analysed,[25,26] the velocities of the pressure front and shear front are 5.24

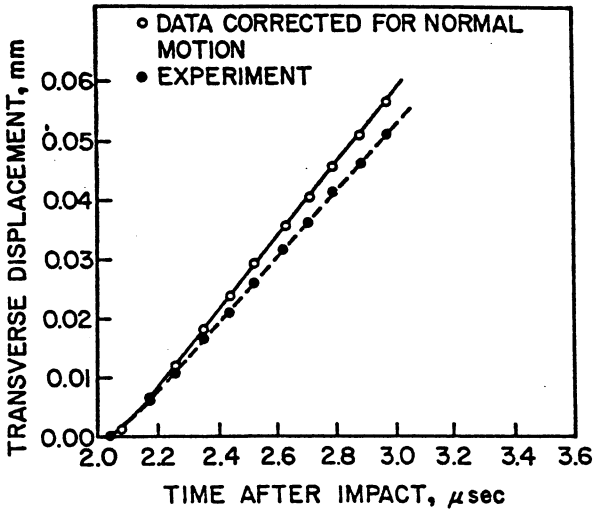

FIG. 2.7 Experimental results obtained by Abou-Sayed *et al.*[27]

and 3.10 mm/μs, respectively. Hence, the plastic shear wave has a velocity slightly higher than half the plastic pressure (shock) velocity. This is about the same ratio as the one obtained between shear and longitudinal elastic waves. Plastic shear waves are certainly of great importance in dynamic deformation.

2.3.4. Additional Considerations on Plastic Waves

The theory of von Kármán and Duwez[5] is only the first step towards an understanding of plastic waves in solids. A considerable theoretical effort has been devoted, over the past twenty years, to develop models for the propagation of plastic waves. At the same time, it has been realized that the hydrodynamic treatment of shock waves is over-simplified and fails to predict a number of phenomena; even at high pressures strength effects are of importance. A number of mathematical formulations have been proposed incorporating the material properties by a constitutive equation. These relationships are, for the most part, non-linear. Lee[38] developed a theory which he called elasto-plastic with finite deformation. Hermann and Nunziato[9] divide the response into several categories, depending on the wave-propagation characteristics, and analyse them in terms of linear viscoelastic infinitesimal elastic-perfectly plastic, non-linear viscoelastic, and thermoelastic, behaviors. Clifton[39] and Hermann,[7] describe the analytical approach, and a recent report by the National Materials Advisory Board[41] makes a critical analysis of the state of the art and of the areas that need development.

An experimental technique that has been used often to obtain con-

stitutive relations at high strain rates is the split Hopkinson bar. It is, in its present form, a modified version of the bar originally used by Hopkinson,[42] Davies,[43] and Kolsky,[44] who were responsible for its development (see Chapter 4).

2.3.5. Adiabatic Shear Bands

Adiabatic shear bands are a common feature of dynamic deformation. They are not generated by shock waves but have been reported in a range of high-strain-rate deformation processes, such as ballistic impact, high-velocity forming and forging, explosive fragmentation and machining. They consist of narrow bands where intense shearing took place and the effect can be qualitatively explained as follows. Plastic deformation generates heat. As the temperature of the deformed region increases, its flow stress decreases. This leads to a concentration of the deformation along that region, with further heat generation. This self-accelerating process might lead to eventual melting. Morphologically, adiabatic shear bands can be of two types: 'deformation' bands and 'transformation' bands. The latter ones are usually observed in steel, and etch as white streaks in metal. It seems that their structure is different from that of the surrounding material, and attempts (so far, unsuccessful) have been made to identify it.[41] It is composed of very small grain sizes (0.1–1 μm). There is evidence for four possibilities: ferrite (BCC), martensite (BCT), austenite (FCC), and an unnamed BCC phase with a lattice parameter smaller than the normally encountered ferrite. It is certain that adiabatic shear bands are present in high-energy-rate fabrication processes such as explosive forming, welding, and even compaction. Virtually nothing is known about the micromechanical deformation processes leading to thermoplastic band formation. The mechanical aspects and requirements will be very briefly reviewed here.

Zener and Hollomon[83] were the first to report these bands. They suggested that they would form when the decrease in flow stress, due to temperature rise, offset the increase in flow stress due to work hardening. Recht, in 1964,[84] expressed this criterion in a more quantitative way, starting from a simplified mechanical equation of state:

$$\sigma = f(\varepsilon, T),$$

$$\mathrm{d}\sigma = \left(\frac{\partial \sigma}{\partial \varepsilon}\right)_T \mathrm{d}\varepsilon + \left(\frac{\partial \sigma}{\partial T}\right)_\varepsilon \mathrm{d}T$$

where σ is the shear stress, and ε and T are the strain and temperature,

respectively. Recht assumed that catastrophic (unstable) flow would occur when $d\sigma/d\varepsilon$ would become equal to zero; or:

$$\left(\frac{\partial\sigma}{\partial\varepsilon}\right)_T = -\left(\frac{\partial\sigma}{\partial T}\right)_\varepsilon \frac{dT}{d\varepsilon} \tag{2.53}$$

He derived an expression for the increase in temperature with strain for a narrow band of thickness t, in a block of thickness L, of the form:

$$\frac{dT}{d\varepsilon} = \frac{\sigma_y L}{2W}\left[\frac{\dot{\varepsilon}}{\pi k\rho c(\varepsilon-\varepsilon_y)}\right] \tag{2.54}$$

where σ_y and ε_y are the stress and strain of yield (initial), k is the thermal conductivity, W is the work equivalent of heat, c is the specific heat, and ρ is the density. Substituting eqn. (2.54) into eqn. (2.53) one arrives at the critical strain rate:

$$\dot{\varepsilon}_c = 4\pi k\rho c(\varepsilon-\varepsilon_y)\left[\frac{\left(\frac{\partial\sigma}{\partial\varepsilon}\right)_T}{\left(\frac{\partial\sigma}{\partial T}\right)_\varepsilon}\right]\frac{W^2}{\sigma_y^2 L^2} \tag{2.55}$$

More sophisticated criteria have been proposed but Recht's analysis seems to predict the correct trends. Additional work on adiabatic shear bands is reported in references 85 to 88 and reference 21.

An interesting concept that was recently introduced[87] is wave trapping. One can see from eqn. (2.48) that the wave velocity varies with the square root of the work-hardening rate. Thus, when $d\sigma/d\varepsilon \rightarrow 0$, the plastic wave should cease to propagate, and deformation will become localized.

The authors would like to speculate on a mechanism for the formation of 'transformation' shear bands. These regions, also called 'white streaks', would be due to localized melting caused by high levels of strain and/or fracture. The solid metal surrounding the molten layer is an almost ideal heat sink and, once the deformation is completed, would provide very high cooling rates. Recent studies on rapidly-solidified metals[40] show that one has the following sequence of morphologies; as the cooling rate is increased: microdendritic structure, microcrystalline structure and amorphous structure. The microcrystalline structure requires cooling rates of 10^4 K s^{-1} or higher. Concomitant with melting, one would have dissolution of the carbides; during subsequent solidification, there would be no time for segregation and a supersaturated solution of carbon in iron would result. This, combined with the extremely small grain size (of

the order of fractions of a micrometer) would be responsible for the high hardness.

2.4. SHOCK WAVES

Shock waves are characterized by a steep front, and require a state of uniaxial strain which allows the build-up of the hydrostatic component of stress to high levels. When this hydrostatic component reaches levels that exceed the dynamic flow stress by several factors, one can, to a first approximation, assume that the solid has no resistance to shear ($G=0$). The treatment developed by Hugoniot and Rankine for fluids is commonly applied to the treatment of shock waves.

2.4.1. Hydrodynamic Treatment

The calculation of shock-wave parameters is based, in its simplest form, on the Rankine–Hugoniot[45,46] equations. Essentially, it is assumed that the shear modulus of the metal is zero and that it responds to the wave as a liquid. Hence, the theory is restricted to higher pressures. At pressures close to the dynamic yield strength of metals, more complex computations have to be used. However, it will suffice here to derive the equations for hydrodynamic behavior. The *fundamental* requirement for the establishment of a shock wave is that the velocity of the pulse increases with increasing pressure. This is shown in Fig. 2.3(b). The velocity of the front will be that of the particles subjected to the highest pressure.

Ahead of the front, the pressure is P_0 and density ρ_0; behind they are P and ρ respectively. The velocity of the front is U_s; the particles (or atoms) are stationary ahead of the front. At the front and behind it, they are moving at a velocity u_p. This displacement of the particles is responsible for the pressure build-up. If one considers the center of reference as the shock front and moving with it, and sets up the equation for the conservation of mass, one has: material moving towards front: $A\rho_0 U_s dt$, material moving away from front: $A\rho(U_s-u_p)dt$. Hence

$$\rho_0 U_s=\rho(U_s-u_p) \tag{2.56}$$

The conservation of momentum can be expressed likewise.

$$\text{Unit impulse}=(\text{momentum in}-\text{momentum out})=(\rho_0 U_s dt\, A)u_p$$

Where $\rho_0 U_s dt A$ is the mass, while u_p is the particle velocity change. The

impulse is

$$(P_0 - P)\mathrm{d}tA$$

Hence

$$(P - P_0) = \rho_0 u_p U_s \tag{2.57}$$

The quantity $\rho_0 u_p U_s$ is usually called the shock impedance. The conservation of energy is obtained by setting up an equation in which the work done is equal to the difference in the total energy of the two sides.

$$A\mathrm{d}t(Pu_p - \mathrm{P}_0 \times 0) = 1/2mu_p^2 A\,\mathrm{d}t + mA\,\mathrm{d}t(E - E_0)$$

$$Pu_p = 1/2\rho_0 U_s u_p^2 + \rho_0 U_s(E - E_0) \tag{2.58}$$

where E and E_0 are the internal energies.

However, since there are five variables in eqns. (2.56) to (2.58) an additional equation is needed. This fourth equation is experimentally determined and is given as a relationship between shock and particle velocities.

$$U_s = C_0 + S_1 u_p + S_2 u_p^2 \tag{2.59}$$

S_1 and S_2 are empirical parameters and C_0 is the sound velocity in the material at zero pressure. For most metals $S_2 = 0$ and eqn. (2.59) is reduced to

$$U_s = C_0 + S_1 u_p \tag{2.60}$$

With the knowledge of the values of C_0 and S_1 for a given material and applying eqns. (2.56), (2.57), (2.58) and (2.60), it is possible to calculate the required quantities.

Figure 2.8(a) shows that U_s versus u_p curve for nickel; as expected, the relationship is linear. By applying eqns. (2.56) to (2.58) one can plot the pressure versus the volume (V/V_0) (Fig. 2.8(b)), and versus the particle velocity (u_p), as shown in Fig. 2.8(c). Specific information on the design of shock recovery systems is given by deCarli and Meyers.[29] Three good sources of information are refs. 47 to 51.

The Mie–Grüneisen–Debye theory is well known for its application in a somewhat more refined treatment of shock waves. The Mie–Grüneisen equation of state is:

$$P = P_k(V) + NkT\Gamma(V)D(\theta/T)/V + (2/3)\alpha V^{-1/3}T^2 \tag{2.61}$$

where $D(\theta/T)$ is the Debye function, $\Gamma(V)$ is the Grüneisen parameter and other symbols have their usual value.

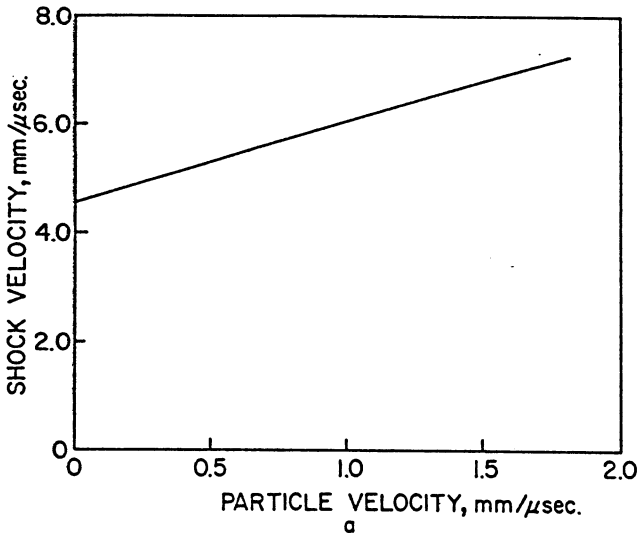

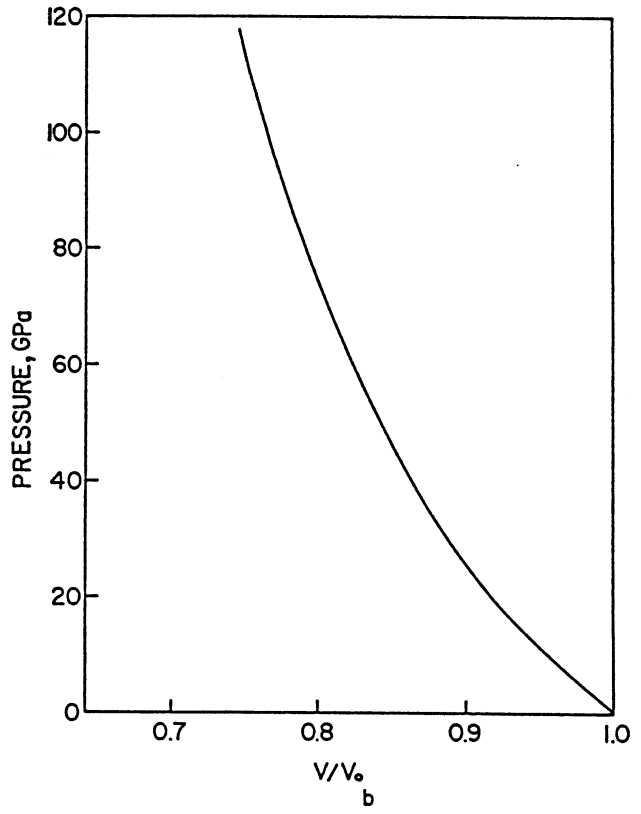

FIG. 2.8 (a) Particle velocity versus shock velocity for nickel (adapted from Meyers[53]). (b) Hugoniot curve for nickel (adapted from Meyers[53]). (c) (overleaf) Pressure versus particle velocity for nickel (adapted from Meyers[53]).

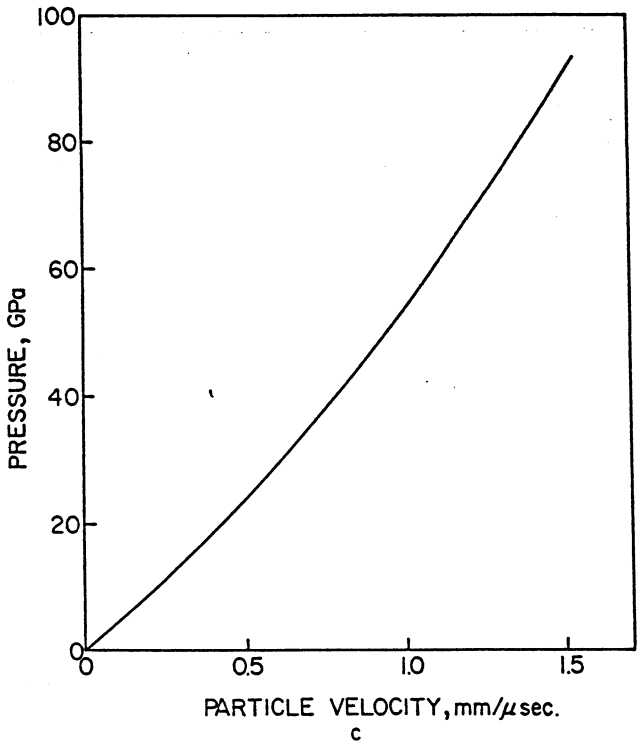

c

FIG. 2.8 *contd.*

In order to obtain the pressure generated by an impact of a flyer plate on a target plate at a known velocity, one plots the pressure, P, versus particle velocity, u_p, for both materials and applies the impedance matching technique, as described in reference 29. The equations required to obtain the density (ρ), the compressibility ratio (V/V_0), the shock velocity (U_s), and particle velocity (u_p) can be obtained by manipulating the Rankine–Hugoniot relations (eqns. (2.56), (2.57), (2.58), (2.60)). The coefficients in the empirical linear relationship between u_p and U_s are taken from Table C-1 (ref. 21). The sound velocity C as a function of pressure was obtained from eqn. (33) in ref. 52.

$$C^2 = -V^2 \frac{dP_H}{dV}\left[1 - \frac{\gamma}{V}\frac{V_0 - V}{2}\right] + V^2 \frac{\gamma}{V}\left[\frac{P_H - P_0}{2}\right] + V^2 (P - P_H)\left[\frac{\gamma}{V} + \frac{d \ln (V/\gamma)}{dV}\right] \quad (2.62)$$

The two derivatives can be evaluated and are:

$$\frac{dP_H}{dV} = \frac{-\rho_0^2 C_0^2}{[1 - S(1 - \rho_0 V)]^2} - \frac{2S\rho_0^2 C_0^2 (1 - \rho_0 V)}{[1 - S(1 - \rho_0 V)]^3} \quad (2.63)$$

$$\frac{\mathrm{d}\ln(V/\gamma)}{\mathrm{d}V}=\left(\frac{\gamma}{V}\right)\mathrm{d}\left(\frac{V}{\gamma}\right)/\mathrm{d}V=\frac{1}{V} \tag{2.64}$$

where γ is the Grüneisen constant and P_H is the pressure at the Hugoniot. Table 2.2 presents the shock wave parameters for a number of metals at the pressures of 10, 20, 30, 40 GPa. The values of γ were taken from ref. 52.

When the solid being shocked undergoes a pressure-induced phase transformation, the P versus V/V_0 plot exhibits a discontinuity in the slope. Figure 2.9(a) shows this effect for iron. At 13 GPA iron undergoes an α(BCC)$\rightarrow\varepsilon$(HCP) transformation. Upon unloading, the reverse transformation does not occur at the same pressure, producing the hysteresis behavior shown. Duvall and Graham[54] have presented a comprehensive treatment of shock-induced phase transformations. The velocity of the shock wave is proportional to the square root of the slope of the Raleigh line. The Raleigh line is defined as the line passing through the points $(V/V_0, P)$ and $(1,0)$. Two Raleigh lines R_1 and R_2, corresponding to pressures P_1 and P_2, are shown in Fig. 2.9. One can see that the slope of R_2 is lower than R_1, although $P_2>P_1$. Hence, the wave will decompose itself into two waves, as shown in Fig. 2.9(b).

The rarefaction—or release—part of the shock wave is the region beyond the peak pressure, where the pressure returns to zero. The attenuation of a wave, on the other hand, is the decay of the pressure pulse as it travels through the material. Figure 2.10 shows schematically how a shock wave is changed as it progresses into the material. At t_1, the wave has a definite peak pressure, pulse duration and rarefaction rate (mean slope of the back of the wave). The inherent irreversibility of the process is such that the energy carried by the shock pulse continuously decreases. This is reflected by a change of shape of the pulse. If one assumes a simple hydrodynamic response of the material, the change of shape of the pulse can be simply seen as the effect of the differences between the velocities of the shock and rarefaction part of the wave. It can be seen in Fig. 2.10 that the rarefaction portion of the wave has a velocity u_p+C, where u_p is the particle velocity and C the sound velocity at the pressure. As the wave progresses, the rarefaction part of the wave overtakes the front, because $u_p+C>U_s$. This will reduce the pulse duration to zero. After it is zero, the peak pressure starts to decrease. As this peak pressure decreases, so does the velocity of the shock front: $U_{s4}<U_{s3}<U_{s2}=U_{s1}$. This can be easily seen by analysing the data in Table 2.2. By appropriate computational procedures one can calculate the change in pulse shape based on the velocities of the shock and

TABLE 2.2

SHOCK-WAVE PARAMETERS FOR SOME REPRESENTATIVE METALS (ADAPTED FROM REF. 21)

Pressure GPa	ρ g/cm^3	V/V_0	U_s *km/s*	u_p *km/s*	C *km/s*
2024 Al					
0	2.785	1.0	5.328	0.0	5.328
10	3.081	0.904	6.114	0.587	6.220
20	3.306	0.842	6.751	1.064	6.849
30	3.490	0.798	7.302	1.475	7.350
40	3.647	0.764	7.794	1.843	7.774
Cu					
0	8.930	1.0	3.940	0.0	3.94
10	9.499	0.940	4.325	0.259	4.425
20	9.959	0.897	4.656	0.481	4.808
30	10.349	0.863	4.950	0.679	5.131
40	10.668	0.835	5.218	0.858	5.415
Fe					
0	7.85	1.0	3.574	0.0	3.574
10	8.479	0.926	4.155	0.306	4.411
20	8.914	0.881	4.610	0.550	5.054
30	9.258	0.848	4.993	0.759	5.602
40	9.543	0.823	5.329	0.945	6.092
Ni					
0	8.874	1.0	4.581	0.0	4.581
10	9.308	0.953	4.916	0.229	5.005
20	9.679	0.917	5.213	0.432	5.357
30	9.998	0.888	5.483	0.617	5.661
40	10.285	0.863	5.732	0.786	5.933
304SS					
0	7.896	1.0	4.569	0.0	4.569
10	8.326	0.948	4.950	0.256	5.051
20	8.684	0.909	5.283	0.479	5.439
30	8.992	0.878	5.583	0.681	5.770
40	9.264	0.852	5.858	0.865	6.061
Ti					
0	4.528	1.0	5.220	0.0	5.220
10	4.881	0.928	5.527	0.4	5.420
20	5.211	0.869	5.804	0.761	5.578
30	5.525	0.820	6.059	1.094	5.708
40	4.826	0.777	6.296	1.403	5.815
W					
0	19.224	1.0	4.029	0.0	4.029
10	19.813	0.970	4.183	0.124	4.207
20	20.355	0.944	4.326	0.240	4.365
30	20.849	0.922	4.462	0.350	4.508
40	21.331	0.901	4.590	0.453	4.638

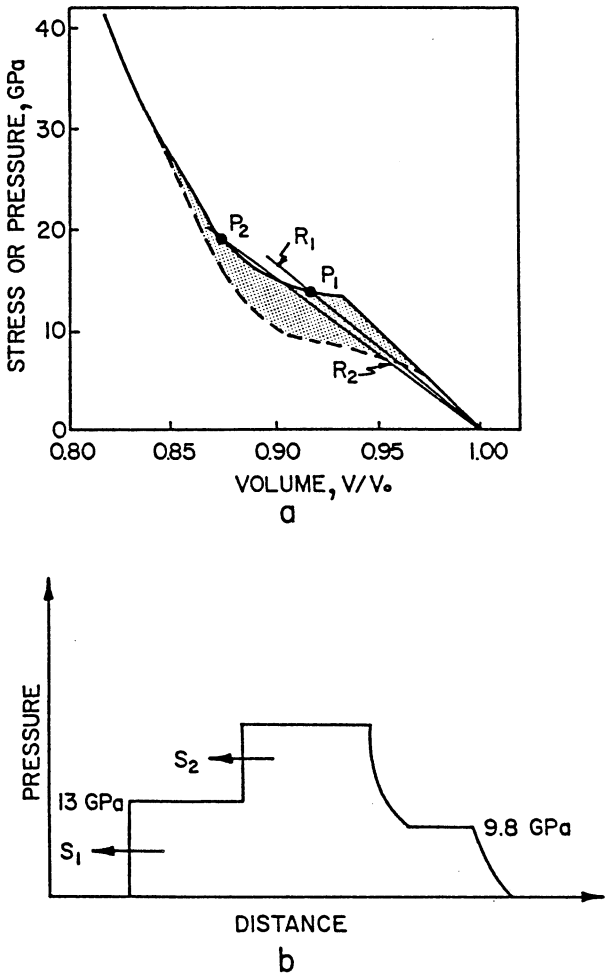

FIG. 2.9 (a) Pressure versus volume (V/V_0) for iron, showing the effects of transformation. (b) Shock pulse configuration for iron above 13 GPa.

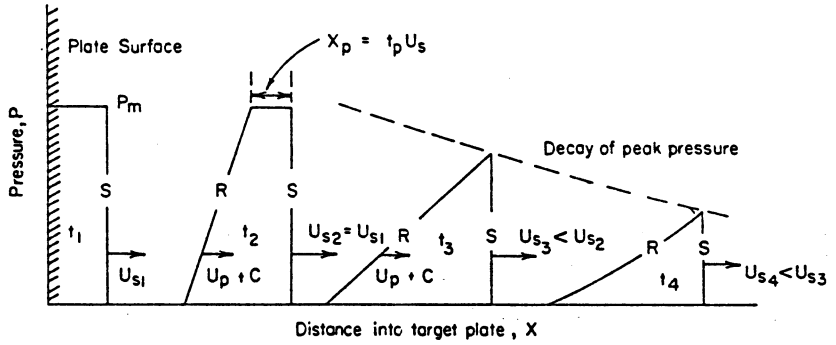

FIG. 2.10 Progress of a shock pulse through metal; rarefaction front steadily overtakes shock front.

rarefaction portion of the wave. This is done below, in a very simplified manner. In order to calculate the rarefaction rate of the pressure pulse as it enters the material, it is best to use Fig. 19 of ref. 29. The rarefaction rate is the slope of the wave tail. Although the curve is concave upwards, we can, as a first approximation, assume it to be a straight line and calculate an average dP/dt. The average rarefaction rate can be obtained by dividing the peak pressure by the difference between the time taken for the head and the tail of the rarefaction wave to pass through a certain point. The head and tail of the rarefactions are shown and travel with velocities u_p+C and C_0, respectively. If one wants to determine the rarefaction rate at the collision interface, one has to find the difference t_3-t_2. One should notice that when the flyer plate is under compression, its thickness is ρ_0/ρ. Hence

$$t_3-t_2=t^F\left(\frac{\rho_0}{\rho}\right)\left(\frac{1}{c}\right)-t^F\left(\frac{1}{c_0}\right) \tag{2.65}$$

$$\dot{P}=\frac{dP}{dt}=P_m\left[t^F\left(\frac{\rho_0}{\rho c}-\frac{1}{c_0}\right)\right]^{-1} \tag{2.66}$$

The rate of rarefaction is very sensitive to pressure. So, if either the impact velocity or the flyer-plate thickness is changed, for the same target-projectile system, different rarefaction rates will result.

The attenuation rate (or decay rate) measures the rate at which the pressure pulse dissipates itself as it travels through the material. The energy carried by the pressure pulse is dissipated as heat, defects generated, and other irreversible processes. Figure 2.10 shows schematically how the energy carried by the wave decreases as it travels from the front to the back face of the target. Up to a certain point the pressure remains constant; it can be seen that at t_3 the pressure has already decreased from its initial value and that at t_4 it is still lower. The greater the initial duration of a pulse, the greater will be the energy carried by it, and consequently, its ability to travel throughout the material. The simplest approach to calculating the decay rate of a pulse is to assume the hydrodynamic response of the material. As illustrated in Fig. 2.10 the relative velocities of the shock and release waves will determine the attenuation. The head of the release wave travels at a velocity u_p+C; the distance that the peak pressure is maintained is given by the difference between the shock velocity U_s and u_p+C. Hence:

$$S=\frac{t_p U_s^2}{u_p+C-U_s} \tag{2.67}$$

Beyond this point numerical techniques have had to be used to compute the pressure decay. This can be done in an approximate way by drawing the pulse shape at fixed intervals, assuming the shock-wave velocity constant in each of them.

2.4.2. More Advanced Treatments and Computer Codes

The hydrodynamic theory refers only to pressures, since it assumes that $G=0$ and that the material does not develop shear stresses. However, the state of uniaxial strain generates shear stresses, and these cannot be ignored in a more detailed account.

One can define the pressure as the hydrostatic component of the strain:

$$dP=\frac{E}{3(1-2\nu)}d\varepsilon_1$$

Assuming that E and ν are not dependent upon pressure, one has:

$$P=\frac{E}{3(1-2\nu)}d\varepsilon_1$$

The maximum shear stresses can be obtained from the deviatoric stresses, which are given with respect to their principal axes:

$$\tau_{max}=\frac{\sigma_1-\sigma_3}{2}=\frac{3(1-2\nu)}{2(1+\nu)}P \tag{2.68}$$

The derivation is given in greater detail by Meyers and Murr.[55]

The recognition of the existence of material strength has led to a number of proposals. Another great problem in the mathematical treatment of shock waves is the discontinuity in particle velocity, density, temperature and pressure across the shock front. The differential equations describing these processes are non-linear and trial-and-error computations are required at each step (in time). For this reason, von Neumann and Richtmyer[56] proposed in 1949 a method for treatment of shock waves which circumvented these discontinuous boundary conditions, and, as a result, lent itself much better to mathematical computations. In essence they introduced an *artificial viscosity* term. This artificial viscosity term had the purpose of smoothing the sharp shock front and rendering it tractable in differential equations and finite difference techniques. The shock front was made somewhat larger than the grid in the finite element network. The physical explanation for the

introduction of a viscosity form[56] is reasonable: dissipative mechanisms take place at the shock front and they can be represented by a mathematical viscosity term. Hsu *et al.*[68] studied in detail the specific dissipative mechanisms. These are discussed in the next section. The artificial term used by von Neumann and Richtmyer[56] was:

$$q = -\frac{(c\Delta x)^2}{V}\frac{\partial u_p}{\partial x}\left|\frac{\partial u_p}{\partial}\right| \tag{2.69}$$

where x designates the position in Lagrangian coordinates, and u_p is the particle velocity.

The differential equations describing the progress of a shock wave can be second-order partial ones. If there are two independent variables (for example, the position, x, and the time, t), one has a hyperbolic differential equation if two characteristic curves pass through each point of the space. A detailed description of the method of characteristics is given by Karpp and Chou.[19] These characteristic curves are obtained from characteristic directions. The application of finite difference techniques to these characteristic curves produces what is known as 'the method of characteristics'. In its graphical representation, one sees two fans of characteristic curves mutually normal. The shock-wave parameters can be determined at these points. Figure 2.11 shows an example.[57] The detonation of an explosive (at grazing incidence) in contact with a metal block generates in the latter a pressure pulse, whose front will be curved because the shock-wave velocity depends upon pressure, which decreases as the wave attenuates itself. Figure 2.11(a) shows the situation schematically. The characteristic curves are shown in Fig. 2.11(b). One can determine the state properties of the expanding gas at all intersections of the curves of two families; the pressures within the slab can also be found. This method of analysis lends itself to a variety of problems involving dynamic propagation of disturbances. Specific examples are: the impact of a plate against a target (NIP code), the motion of compressible flat plates and cylinders drawn by detonation waves (ELA code), plane supersonic gas flow and impact of a cylinder on a plate.

An alternative approach is the finite difference method incorporating an artificial viscosity term. Hence, one would have the following example given by Walsh,[18] for the wave equation:

$$\frac{\partial^2 u}{\partial t^2} = c^2\frac{\partial^2 u}{\partial x^2} = c\frac{\partial}{\partial x}\left(c\frac{\partial u}{\partial x}\right)$$

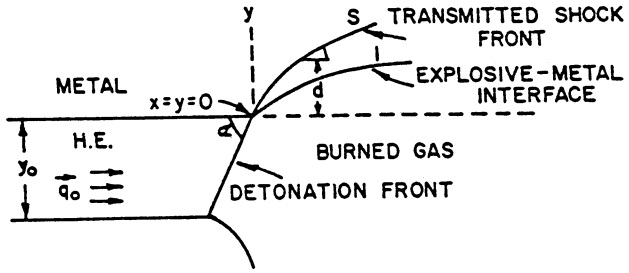

(A)

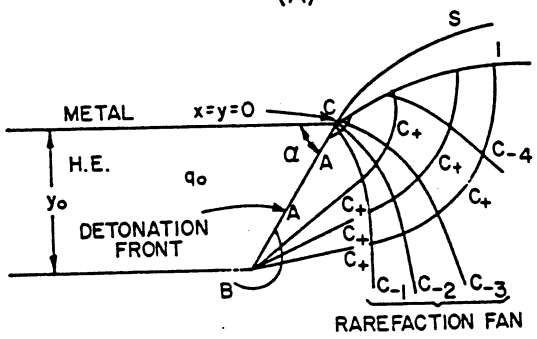

(B)

FIG. 2.11 (a) Detonation of explosive in contact with metal block at grazing incidence. (b) Characteristic fans that are used in the calculation of the state variables at the intersection of the lines, both inside the metal and in the detonation-gases regions (adapted from Drummond.)[57]

Making

$$\sigma = c\frac{\partial u}{\partial x}, \quad \text{and} \quad \omega = \frac{\partial u}{\partial x}$$

One arrives at the equivalent equations:

$$\begin{aligned} \frac{\partial \omega}{\mathrm{d}t} &= c\frac{\partial v}{\partial x}; \\ \frac{\partial v}{\partial t} &= c\frac{\partial \omega}{\partial x} \end{aligned} \tag{2.70}$$

If one expresses these equations in forms of finite differences, one has

$$\frac{\omega_{j+1}^{(n+1)} - \omega_{j+1}^{(n-1)}}{2\Delta t} = c(x_{j+1})\frac{v_{j+2}^{n} - v_{j}^{n}}{2\Delta x};$$

$$\frac{v_{j}^{(n+2)} - v_{j}^{n}}{2\Delta t} = c(x_j)\frac{\omega_{j+1}^{(n+1)} - \omega_{j-1}^{(n+1)}}{2\Delta x}$$

The application of the finite difference method to shocks produces a great deal of 'noise'. The introduction of an artificial viscosity form greatly improves the solution. The coefficient of viscosity smoothes out the pulse; for q^2 equal to 4, the representation is satisfactory. Figure 2.12 shows another example of the propagation of a shock wave as it travels through a metal. This sequence was generated by Wilkins.[16] If residual plastic deformation takes place, one cannot use the hydrodynamic assumption. Wilkins describes the problem in detail. In order to incorporate plastic flow he applies the von Mises yield criterion. Since deformation is three-dimensional, one has a yield surface. For large deformations one can neglect the elastic strains which rarely exceed 0.5 pct. Figure 2.13 shows in sequential form the detonation of composition B explosive in contact with a metal block. Both the expansion of the detonation gases and the propagation of the shock wave into the copper plate can be seen. However, if the hydrodynamic assumption is made (no material strength), the cratering effect is much larger (and not realistic). Hence a yield surface has to be incorporated in this type of problem.

A variety of codes have been developed both with Lagrangian and Eulerian coordinates. Examples of some Lagrangian finite difference codes are TOODY,[58] HEMP,[16] WONDY,[59] while OIL[60] uses Eulerian coordinates. The NAG (nucleation and growth code) was developed by Curran, *et al.*[61] and is intended for the study of spalling. Seaman *et al.*[62] developed a code (PEST) to be used in porous materials.

Although most of these codes have been used exclusively in the development of weapons, warheads, and for gaining a better understanding of nuclear explosions, they could be very helpful in aiding the engineer in high-energy-rate forming applications. The tendency in military research has been to replace a great number of experiments by a few carefully controlled and instrumented tests. Explosive forming, welding and compaction could be simulated in computers, and the problems of wave reflections and spalling could be predicted and avoided. Indeed Hoenig *et al.*[63] have applied the HEMP code to explosive compaction of powders.

2.4.3. Attenuation of Shock Waves

If one looks at a slightly more realistic representation of a shock pulse in a metal, one can distinguish features not represented in Fig. 2.3 and not treated in the hydrodynamic theory. Figure 2.14(a) illustrates such a situation. The material strength is incorporated into the model. The shock pulse is preceded by an elastic precursor wave with amplitude

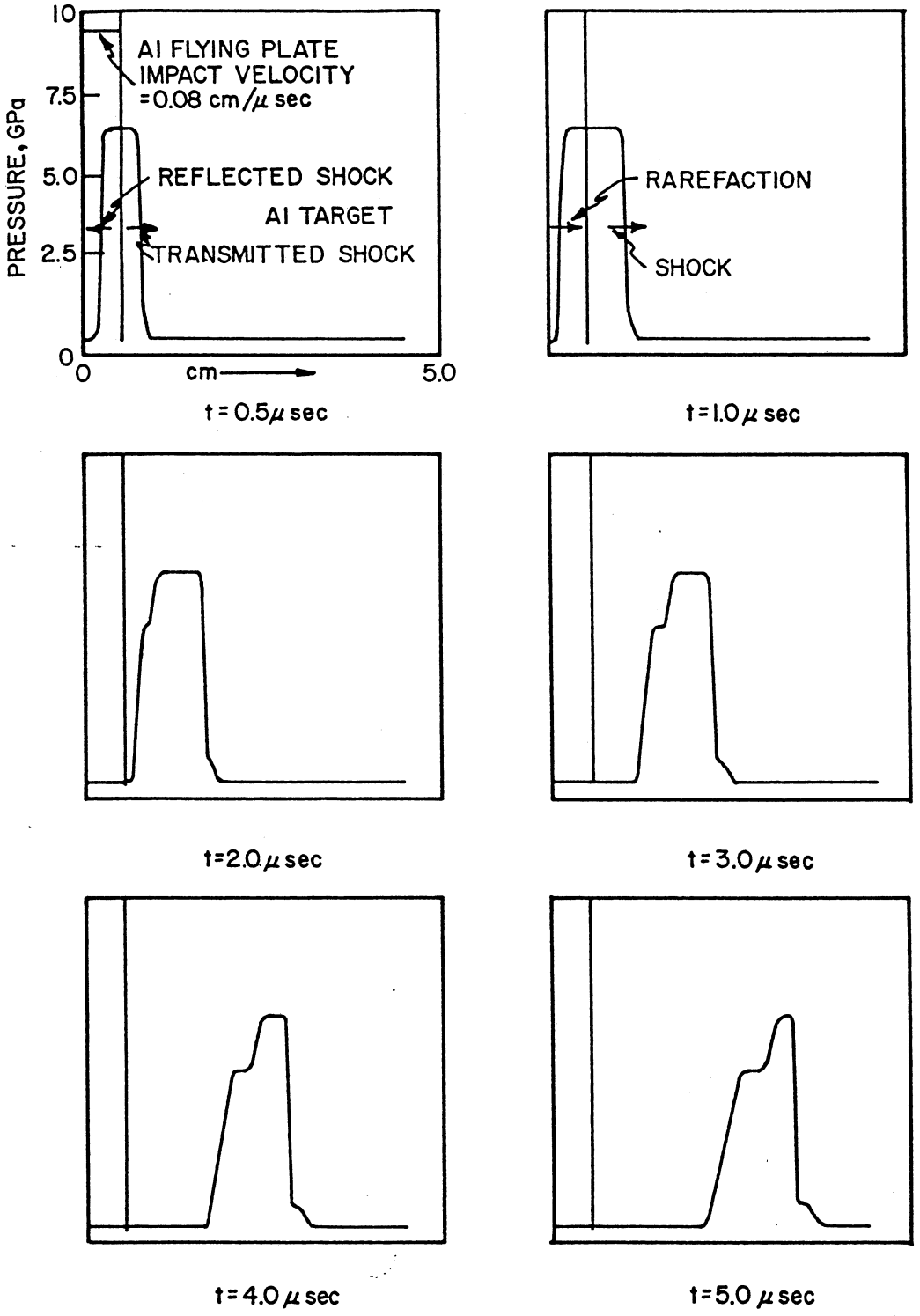

FIG. 2.12 Stress profile produced by the impact of a flyer plate on target, as simulated, using Wilkins[16] code (adapted from ref. 16).

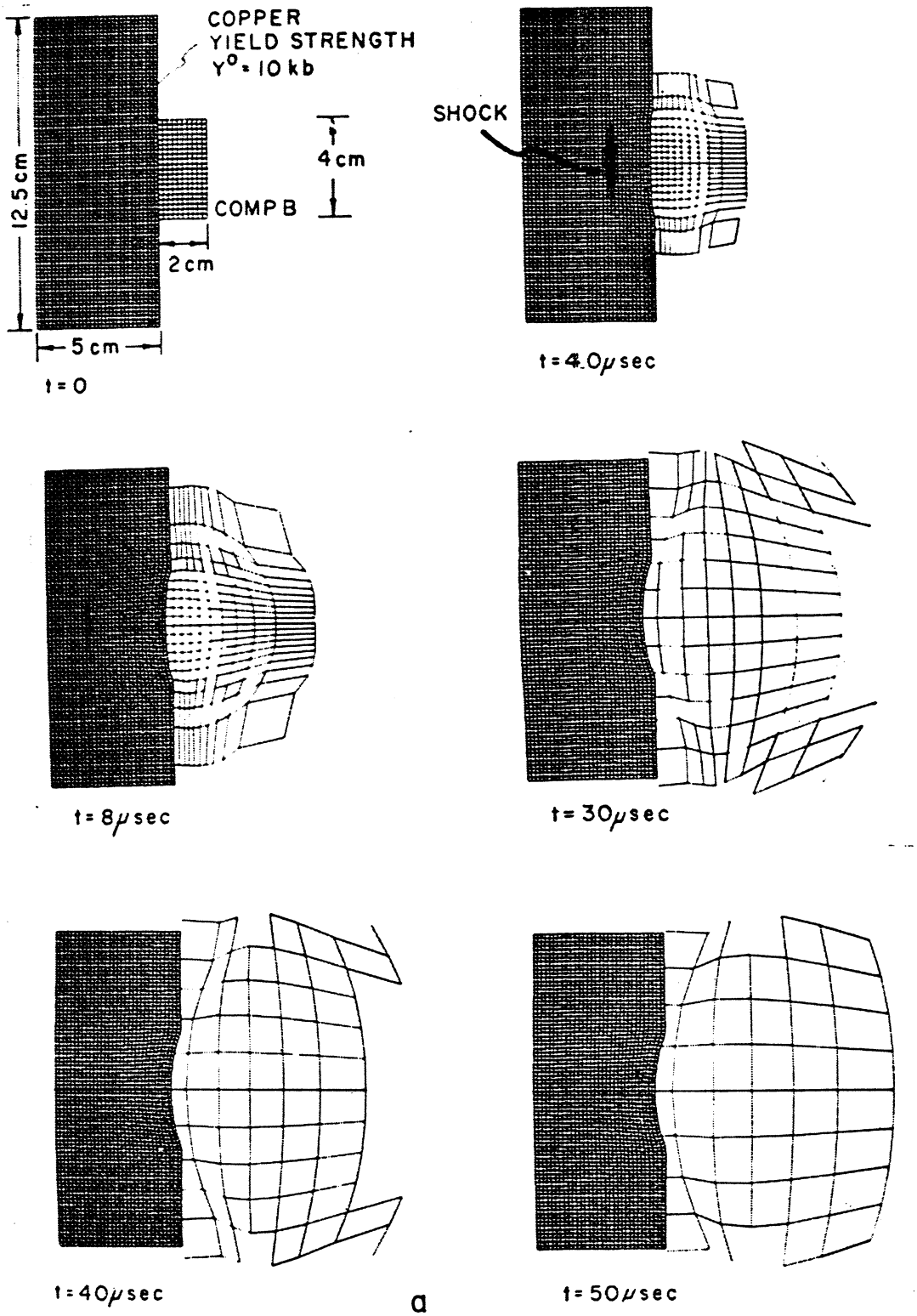

FIG. 2.13 (a) Simulation of detonation of a high explosive (Comp B) in contact with copper block. (b) Same as (a), assuming hydrodynamic behavior (from ref. 16).

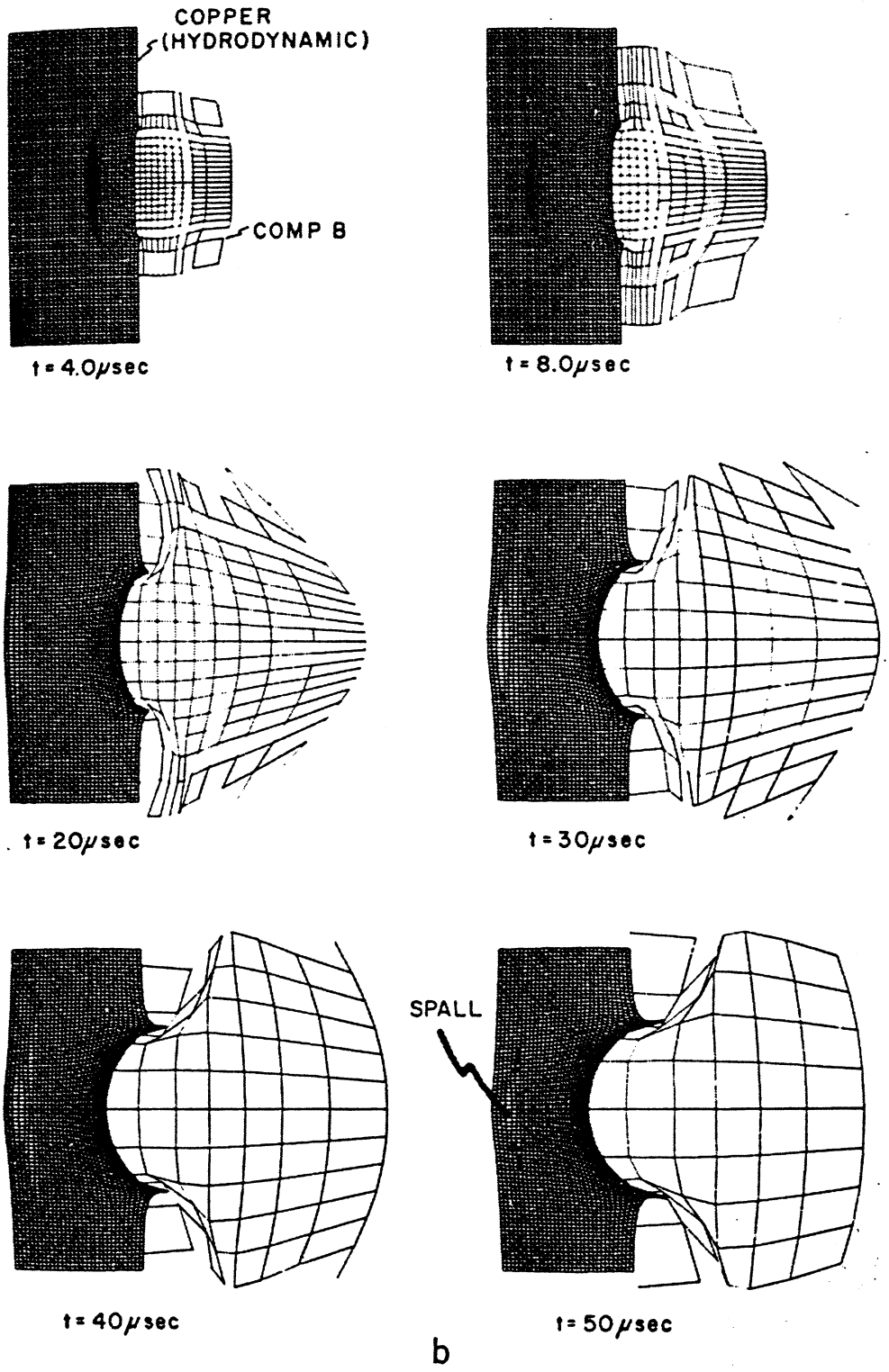

FIG. 2.13 *contd.*

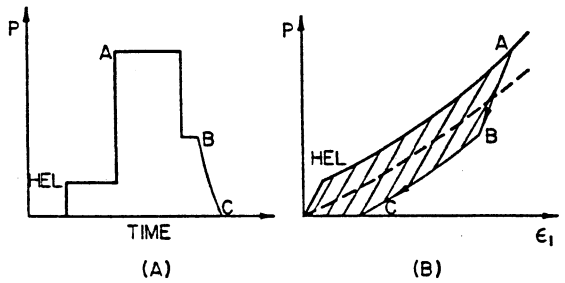

FIG. 2.14 (a) Shock-wave profile including elastic precursor and incorporating strength effects. (b) Pressure versus strain (or volume V/V_0) for hypothetical solid including strength effects; cross-hatched region represents energy dissipated in cycle.

equal to the 'Hugoniot Elastic Limit' (HEL). The rarefaction portion of the wave exhibits a plateau. These two features are better understood if one refers to the pressure versus V/V_0 plot of Fig. 2.14(b). The initial response of the material (at low pressures) is elastic; therefore, it deviates from the hydrodynamic V/V_0 curve. When the Hugoniot elastic limit is reached, the dynamic compressibility curve follows the Hugoniot curve. Taking the slopes of the elastic and plastic curves (Raleigh lines) one can see that the elastic precursor travels faster than the travelling shock waves. It is only for very high pressures that the Raleigh line of the shock pulse has a larger slope than that of the HEL region. Elastic precursors are discussed in Section 2.4.4. Upon unloading, one has first the relieving of the elastic stresses (A to B); then, the curve follows the Hugoniot P versus V/V_0 response up to pressure zero. At point B, the rarefaction part of the wave shows a plateau. The very important feature of Fig. 2.14(b) is the hysteresis behavior. The cross-hatched area indicates the amount of irreversible work done in the process. This irreversibility has a direct bearing on the attenuation of the shock pulse.

Curran[64] and later Erkman *et al.*[65-67] investigated the attenuation of planar shock waves and compared it with the hydrodynamic treatment. They found much higher observed attenuation. This is to be expected, if one looks at the energy dissipated in Fig. 2.14(b). They found a much better agreement incorporating the artificial viscosity into their treatment of shock waves. Rempel *et al.*[66] observed that the pressure starts to decay almost immediately after it propagates, contrary to the hydrodynamic calculations (Section 2.4.2). The problem with the artificial viscosity is that it does not have a clearly defined physical meaning in terms of micromechanical frictional processes. In view of this, Hsu *et al.*[68] recently investigated the attenuation of shock waves in nickel and proposed a

model incorporating defect generation and motion. Figure 2.15 shows the calculated (hydrodynamic theory) and observed peak pressures at varying distances from the peak interface. Two different initial pressures were used: 10 and 25 GPa. The peak pressures observed at 10 cm from the interface are clearly lower than the observed ones. They found no effect of metallurgical variables (substructure and grain size) on the attenuation rate of the pulse. An attempt was made to physically explain the dissipative mechanisms responsible for the attenuation of the pulse. This model is called the 'accumulation model' because it is based on the conservation of energy law:

$$\text{INPUT} - \text{OUTPUT} = \text{ACCUMULATION}$$

The following calculation provides a further understanding. Assume that a shock wave with a peak pressure of 10 GPa and 2 μs pulse duration travels 1 cm through a nickel plate of 1 cm^2 cross-section area. According to the Rankine–Hugoniot theory, one can calculate internal energy per unit volume, E.

In this case, the energy of the incoming pulse with 2 μs pulse duration is 233 J/cm^2. From a metallurgical or microstructural viewpoint, point defects, line defects, twinning, precipitates, martensitic transformations, and heating are dissipative processes causing the attenuation of a shock wave. Since no twinning, precipitation, or phase transformation occurs in the pressure range of 10 and 25 GPa, point and line defect generation, hydrodynamic residual rise in temperature, and temperature rise due to dislocation motion are the significant mechanisms responsible for the attenuation of shock waves in nickel. Dieter[69] estimated the total strain energy of a dislocation to be $1{\cdot}36 \times 10^{-18}$ J per atomic plane. The lattice parameter of nickel is 3.52 A. Multiplying by the dislocation density of 3.1×10^{10} cm/cm^3, the total strain energy of dislocations is 1.2 J/cm^3. The vacancy concentration at 10 GPa is about $3.85 \times 10^5/cm^2$.[70] The formation energy being 1.6×10^{-19} J per vacancy, one obtains 6.2×10^{-14} J/cm^3 for vacancies. This value is so small that it can be neglected. According to the hydrodynamic Rankine–Hugoniot theory, the residual temperature rise is 2 K for nickel at 10 GPa. The heat capacity of nickel is 39 J/cm^3. The thermal energy change is 7.8 J/cm^3. The total accumulation energy above is about 9 J/cm^3. Subtracting this value from the input, one obtains an output of 224 J/cm^2 after the shockwave travels 1 cm within the nickel plate. Figure 2.16 shows a comparison of the 'accumulation model' with the hydrodynamic theory and experimental results.

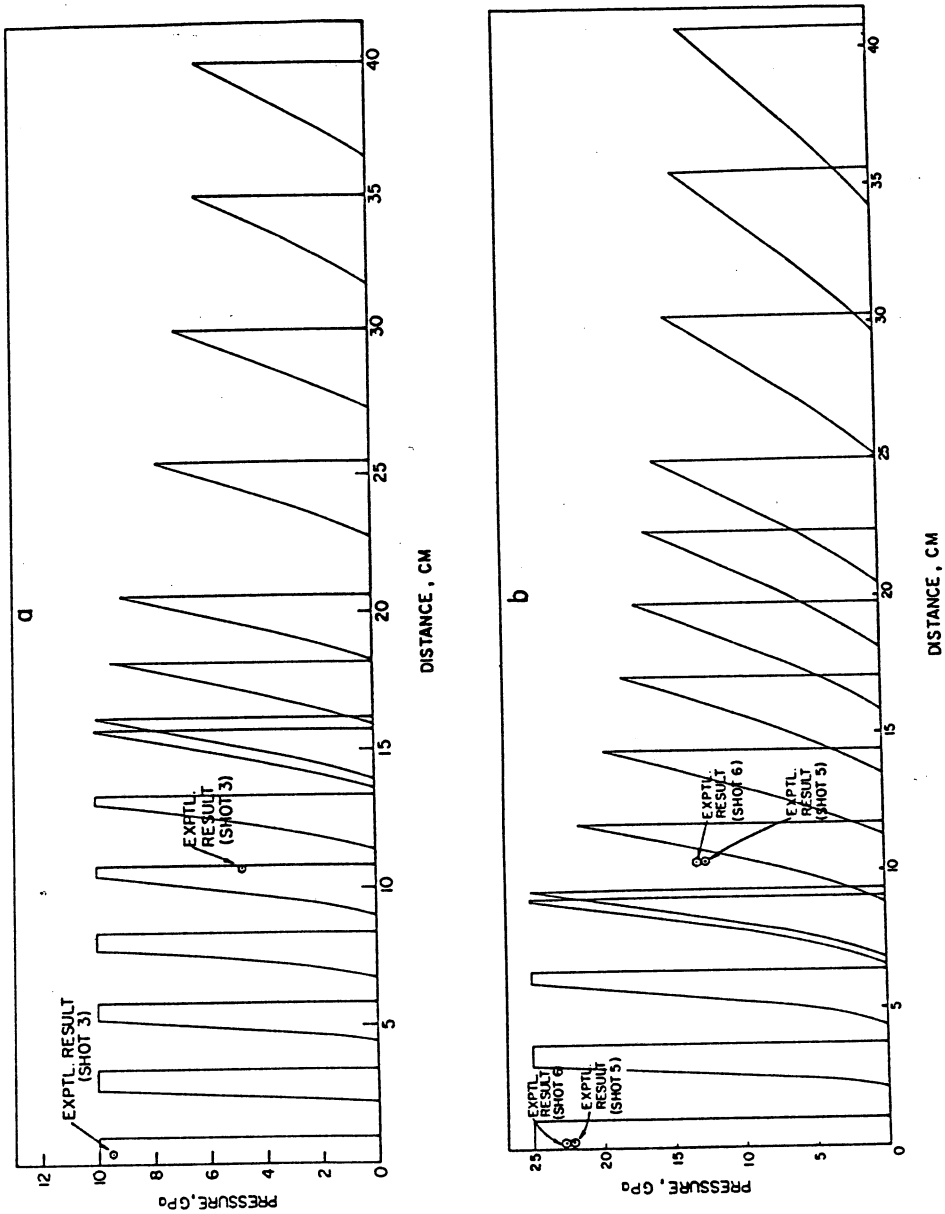

FIG. 2.15 (a) Comparison of attenuation rate predicted by hydrodynamic theory with observations made in model, with manganin piezo-resistive gauges at initial pressure of 10 GPa. (b) Comparison of attenuation rate predicted by hydrodynamic theory with observations made on nickel with manganin piezo-resistive gauges at initial pressure of 25 GPa (from ref. 68).

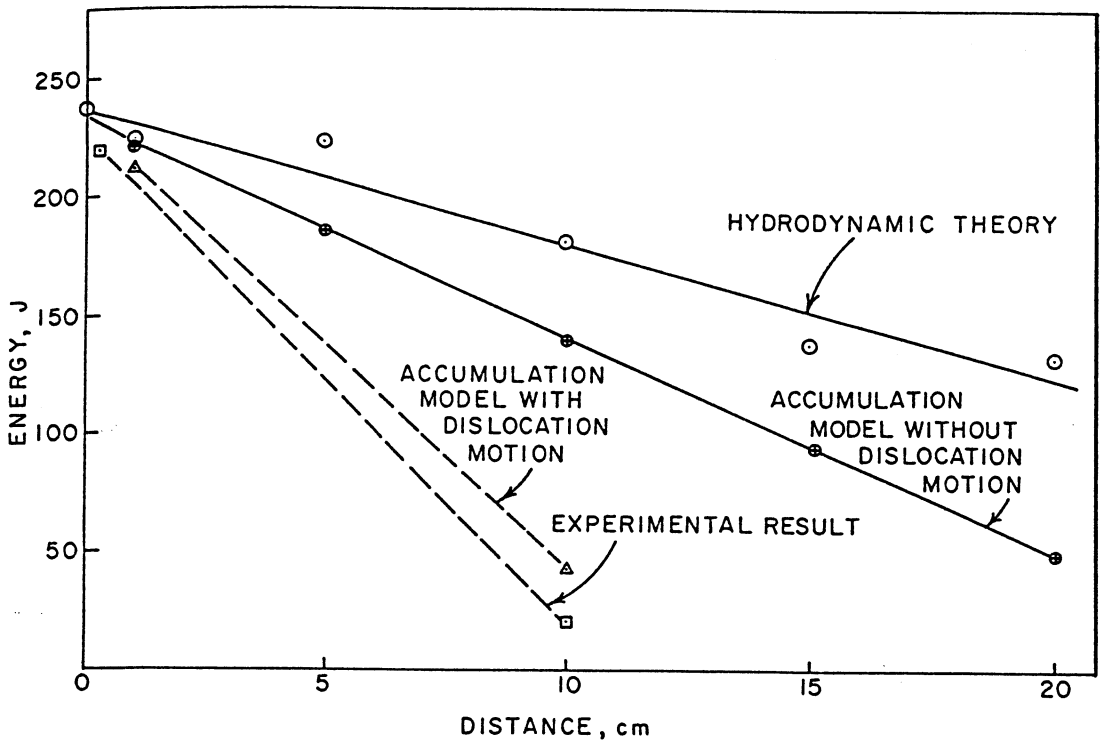

FIG. 2.16 Pulse energy in its downward trajectory (from ref. 68).

One can see that there is still some discrepancy between the 'accumulation' model and the experimental results. This difference is about 120 J at a distance of 10 cm from the top, or an average of 12 J/cm. Hence, dislocation motion was introduced into the model to take into account the additional energy dissipation. This can be done assuming that the work required to move a dislocation is totally converted into heat:

$$W = \tau b l \rho \tag{2.71}$$

where τ is the applied shear stress, b is the Burgers vector (3.5×10^{-10} m), l is the distance moved by each dislocation, and ρ the dislocation density. Setting this work equal to 12 J and assuming, to a first approximation, that each dislocation moves 0.7 μm, one can compute τ; ρ is about 3.1×10^{10} cm^{-2} (Table IV of ref. 68). One finds that τ is approximately 0.16 GPa. From the stress versus velocity plot presented by Meyers (Fig. 4. of ref. 71) for nickel, one can estimate the velocity at which the dislocations would have to move to dissipate the required amount of energy (12 J/cm); it is around 500 m/s. This is clearly a subsonic and reasonable value. Hence, the 'accumulation model' with dislocation motion is in a reasonable agreement with the experimentally determined attenuation of the shock pulse.

2.4.4. Elastic Precursor Waves

As seen in the preceding section, shock waves are preceded by an elastic precursor when their Raleigh slope is less than that of the precursor. At a high enough stress, called 'overdrive stress', the velocity of the shock wave becomes larger than that of the precursor. Figure 2.17 shows the

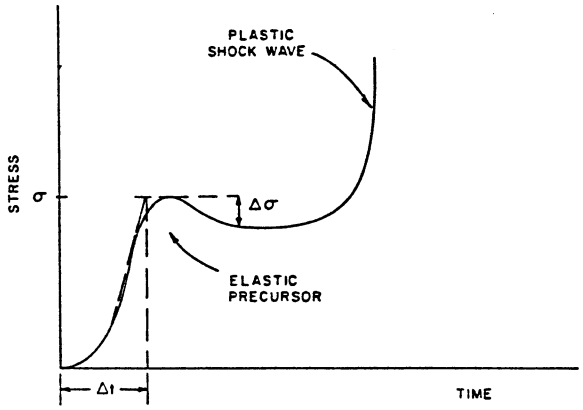

FIG. 2.17 Schematic representation of elastic precursor (from ref. 81).

shape of a general precursor pulse. One has a rise time Δt, a peak stress σ, and a stress drop $\Delta\sigma$. Although the elastic precursor is unimportant in relation to the plastic pulse that succeeds it, it can provide important information on the nature of dynamic deformation. It is for this reason that it has received considerable attention in the past. Davison and Graham[12] provide a comprehensive review of the subject. Some of the work is described below.

Taylor and Rice[72] first observed the decay of the elastic precursor amplitude with depth of penetration into the target; Taylor[73] later explained it successfully in terms of the Johnson–Gilman[74] expression for dislocation velocity. Another feature observed is yield point formation[73,75,76] and, consequently, stress relaxation behind the elastic precursor; Barker *et al.*[75] attributed it to dislocation effects predicted by the Johnson–Gilman model. Kelly and Gillis[77] showed that thermal activation models (e.g., ref. 7) for dislocation dynamics could explain the observed decay behavior as well as the Johnson–Gilman model. Johnson[79] extended the Taylor[73] interpretation of precursor decay to polycrystalline metals. Rohde[80] studied the precursor decay in iron shock-loaded at temperatures ranging from 76 to 573 K and found that the data did not satisfy entirely any of the following models: the Johnson–Gilman model,[74] the activation energy model,[78] or the linear damping model. Meyers[81] studied the effect of polycrystallinity on the

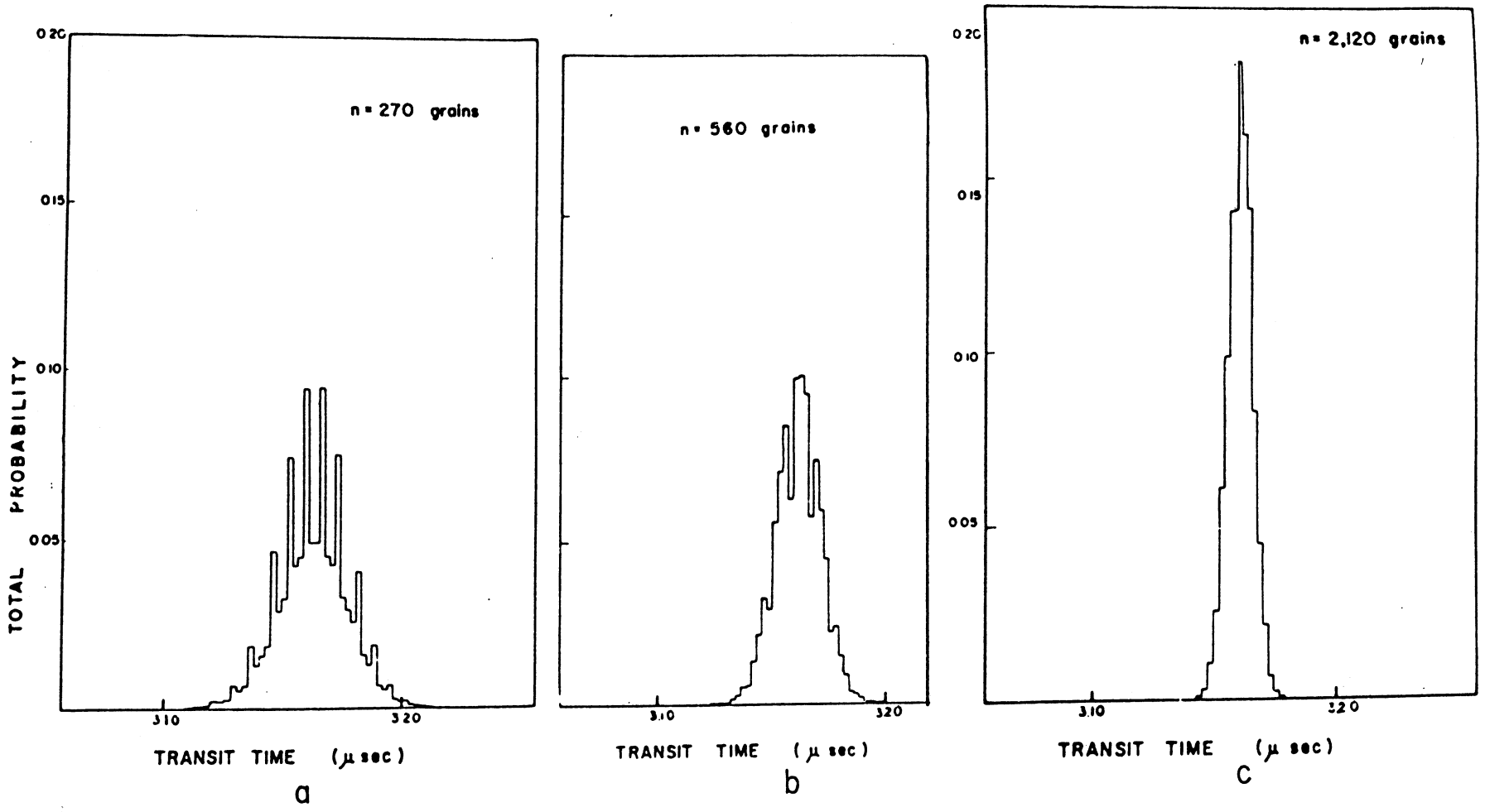

FIG. 2.18 Distribution of transit times of elastic precursor due to velocity anisotropy of the wave, after penetration of 19.05 mm into iron specimen with grain sizes of (a) 70.3, (b) 34, and (c) 9 μm (from ref. 81).

configuration of the elastic precursor wave. Referring to Section 2.2.3, one can see that the velocity of elastic waves is strongly dependent upon crystallographic orientation. Thus, as the precursor travels through different grains of a polycrystalline aggregate, the front undergoes changes as it is reflected at the boundaries and as different parts travel at different velocities. Consequently, the rise time (Δt in Fig. 2.17) is affected; Fig. 2.18 shows how Meyers' model predicts different distributions of the precursor front for different grain sizes, after a distance of 19.05 mm as has been traversed. The greater the grain size, the greater the spread in the front and, consequently, the greater the rise time Δt. This effect is particularly applicable to low shock pressures (<5 GPa) but decreases in significance with peak pressures >5 GPa.

Of great significance from the point of view of fundamental understanding of the behavior of metals, was the discovery by Jones and Holland.[82] The height of the precursor pulse (σ in Fig. 2.17) was found to be independent of grain size. In conventional deformation, on the other hand, the flow stress of iron is significantly dependent upon grain size, the Hall–Petch relationship being the well-known equation relating these two parameters. This finding indicates that the mechanisms of dislocation generation and plastic flow at the precursor front *are different* from those in conventional deformation, and that grain boundaries do not play any significant role.

2.5. DEFECT GENERATION

The reader is referred to ref. 55 for a more in-depth treatment of this section. Metallurgical microdefects are classified into four groups: point, line, interfacial or planar, and volume defects. They are responsible for the great variety of mechanical properties and can be used to strengthen the material. A substantial amount of knowledge and understanding on defect generation and their effects on the mechanical properties of shock-loaded metals has been gained over the past thirty years. The deformation regimes between conventional and shock wave strain rates have not been so exhaustively and systematically investigated. Effects of plastic waves and thermoplastic shear instabilities are not well understood. The detailed mechanical and metallurgical effects are treated in Chapter 3; the fundamental mechanisms are discussed here. Except for this paragraph, the discussion will be restricted to shock waves. An increase in strain rate produces, in general, an increase in flow stress; this is shown in Fig. 3.1 of Chapter 3. Edington[142,143] systematically in-

vestigated the effect of strain rate on the dislocation substructure. For both niobium[143] and copper,[142] he observed the classical flow-stress increase with strain rate increase. He studied the interval 10^{-4}–$10^{3}\,s^{-1}$ for niobium and 10^{-4}–$10^{4}\,s^{-1}$ for copper, using a Hopkinson bar for the higher strain rates. For niobium, he found a more uniform dislocation distribution at $1.5\times10^{3}\,s^{-1}$ than at $1.2\times10^{-4}\,s^{-1}$. On the other hand, for copper no significant difference in the distribution and density of dislocations deformed at $6.5\times10^{3}\,s^{-1}$ and $4\times10^{-4}\,s^{-1}$ was found. In order to understand the effect of strain rate on the final substructure, one has to recognize the importance of the stages leading to this final distribution; dislocation generation, interaction, movement. The dissipative processes involved in dislocation motion are responsible for the requirement of increasingly higher stresses to move the dislocations at increasingly high velocities. The nature of this dependence is very important in establishing the flow stress and the dislocation multiplication and reaction processes. These, in turn, determine the final distribution. In the intermediate velocity range, the velocity of dislocations has been found to be linearly related to the stress:

$$\tau = Bv$$

where B is the damping constant; at ambient temperature phonon 'viscosity' seems to be the principal damping mechanism.

The importance of separating deviatoric from hydrostatic stresses in the treatment of shock waves cannot be over emphasized. Different phenomena are controlled by different stresses. Hence, one has:

Dislocations: generation and motion controlled by deviatoric stresses, stacking-fault energy affected by hydrostatic stresses.

Dispersed particles: they are a source of dislocations due to the different compressibilities; hence, this is an effect of hydrostatic stresses.

Individual grains: in materials that do not exhibit cubic symmetry, individual grains have anisotropic compressibilities and hydrostatic stresses will establish compatibility stresses at their interfaces.

Displacive/diffusionless phase transformation: a number of phase transformations are induced in materials by the hydrostatic component of stress. Martensitic transformation can also be induced by shear stresses or strains.

Twinning: activated by shear stresses. The hydrostatic stresses might have an indirect effect.

Point defects: their generation is due to shear stresses; their diffusion rate is affected by hydrostatic stresses.

Recovery and melting point: affected by hydrostatic stress.

Shock and residual temperatures: affected by both hydrostatic and deviatoric stresses, but for different reasons.

2.5.1. Dislocation Generation

The dislocation substructures generated by shock loading depend on a number of shock-wave and material parameters. Among the shock-wave parameters, the pressure is the most important one. As the pressure is increased, so does the dislocation density.[21] As the dislocation density increases for high stacking-fault energy FCC metals, the cell size decreases. Murr and Kuhlmann-Wilsdorf[90] found that the dislocation density varies as the square root of pressure ($\rho \propto p^{1/2}$). This dependence breaks down at pressures close to 100 GPa, due to shock-induced heating.

The effect of pulse duration has been and remains, to some extent, the object of controversy. Its effect for various alloys is reviewed in reference 91 and discussed in detail in reference 92. Appleton and Waddington[93] were the first to suggest its importance.

The effect of pulse duration is principally to allow more time for dislocation reorganization. The cell walls become better defined as the pulse duration increases, because there is more time for dislocation reorganization. This is shown in Fig. 2.19 which also shows the important microstructural changes, particularly dislocation density, which result when the pressure increases. Experimental observations at very low pulse durations do not seem to be in line with the above rationalization. Marsh and Mikkola[94] have observed that dislocation density increases with increasing pulse duration in the sub-microsecond range. It is possible that these effects are due to subtle pressure variations.

There are some systematic differences and similarities between shock-induced and conventionally-induced dislocations; some of these will be briefly reviewed here. In FCC metals, the stacking-fault energy determines the substructure to a large extent. In any case, however, the dislocations seem to be more uniformly distributed in shock than in conventional deformation. In high-stacking-fault energy alloys, the cell walls tend to be less well-developed after shock loading than after conventional deformation, especially by creep or fatigue, which allow time for dislocations to equilibrate into more stable configurations.

In addition, if the shock pulse duration is low, the substructures are more irregular because there is insufficient time for the dislocations

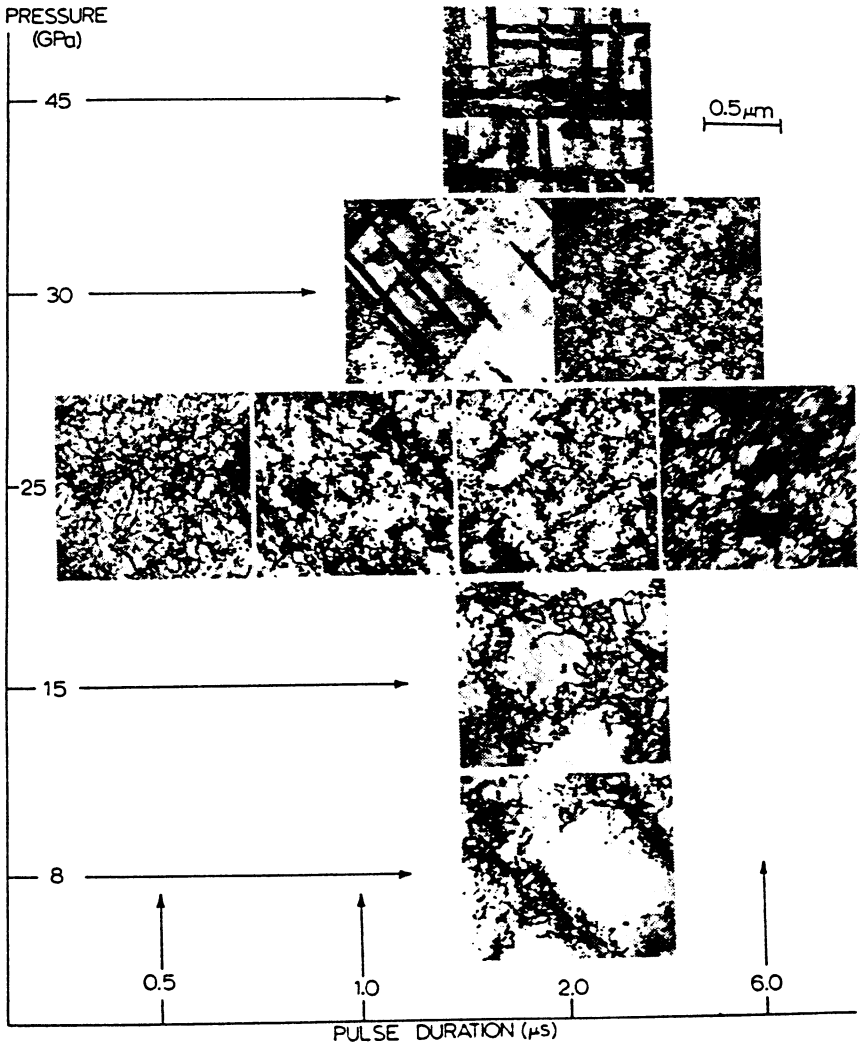

FIG. 2.19 Composite of bright-field electron micrographs showing effect of pressure and pulse duration on the shock-wave response of nickel. All surface orientations are (001), and at 30 GPa, 2 μs both twin and cells exist in (001) orientation. The preponderance of twins also increases in (001) orientations at 30 GPa above 2 μs pulse duration.

generated by the peak pressure (in the shock front) to equilibrate[90] (Fig. 2.19). There is usually a preponderance of dislocation loops associated with the residual shock microstructures, and this is especially unique to shock loading at high stacking-fault free energy metals and alloys. At shock pressures above about 10 GPa, most FCC metals having stacking-fault free energies above about 50 mJ/m^2 tend to exhibit dislocation cell structures as shown in Fig. 2.19. Between 50 and about 40 mJ/m^2 a

transitional range gives rise to tangles of dislocations, poorly formed cells, and sometimes more planar arrays of dislocations (associated with the {111} slip planes).

For lower stacking-fault free energy metals and alloys, there is a tendency toward planar dislocation arrays below about 40 mJ/m^2; with stacking faults and twin faults becoming prominent for stacking-fault free energies below about 25 mJ/m^2. This is illustrated in Fig. 2.20 for nickel and 304 stainless steel shock loaded to the same pressure, at the same pulse duration.

The effect of shock loading on BCC metals is similar to that for nickel in Fig. 2.20(a) but lacks well defined dislocation cells. Shock loaded iron

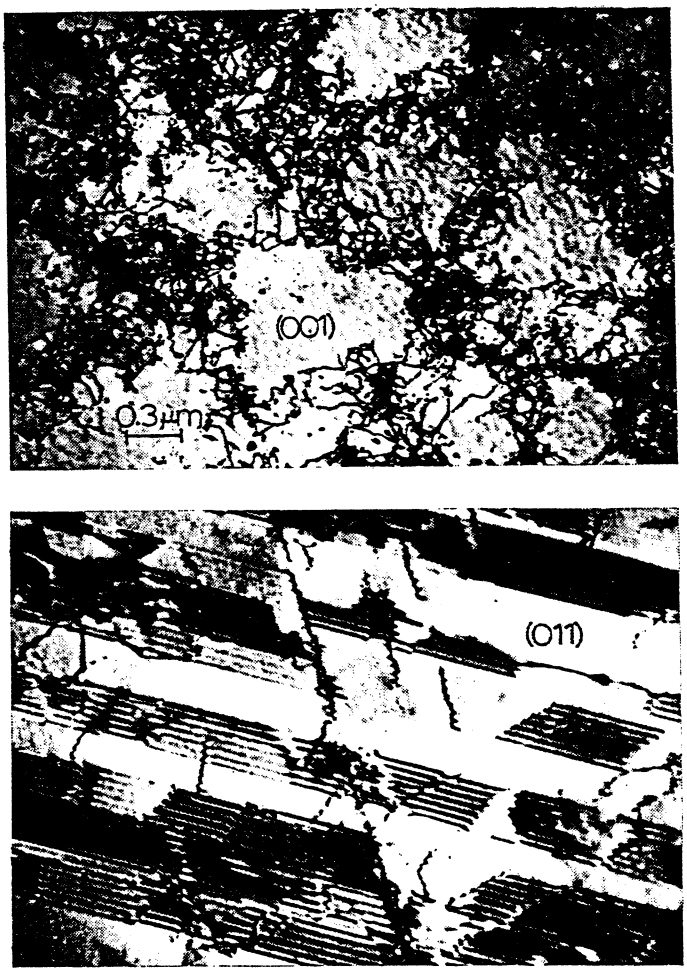

FIG. 2.20 Comparison of substructures in high stacking-fault free energy nickel (128 mJ/m^2) in (a) and in low stacking-fault free energy type 304 stainless steel 21 mJ/m^2) in (b) (15 GPa, $t = 2$ μs).

is characterized, at pressures below 13 GPa, by arrays of straight and parallel screw dislocations, in the properly oriented grains. In molybdenum, the substructure is one of homogeneously distributed dislocations.

Shock loaded HCP metals have not been extensively studied by transmission electron microscopy. Koul and Breedis[96] found, at 7 GPa, dislocation arrays that they described as being intermediary between those of FCC metals such as Cu and Ni, and BCC metals such as iron and Fe_3Al. The substructure also exhibited twins and phase transformations, at higher pressures. Murr and Galbraith[97] studied shock-loaded beryllium which exhibited dislocation substructures similar to those of BCC metals. No twins were observed up to a pressure of 0.9 GPa. A strong dependence of dislocation density was noted for grain boundary structure. This feature is consistent with the establishment of compatibility stresses at the interfaces due to the anisotropy of compressibility, as noted above, giving rise to a preponderance of dislocations from grain-boundary sources as well as alterations in the boundary structure.

The limitations of Smith[98] and Hornbogen's[99] proposals led Meyers[71,100] to propose a model whose essential features are:

(a) Dislocations are homogeneously nucleated at (or close to) the shock front by the deviatoric stresses set up by the state of uniaxial strain; the generation of these dislocations relieves the deviatoric stresses.
(b) These dislocations move short distances at subsonic speeds.
(c) New dislocation interfaces are generated as the shock wave propagates through the material.

This model presents, with respect to its predecessors, the following advantages:

(a) No supersonic dislocations are needed.
(b) It is possible to estimate the residual density of dislocations.

Figure 2.21 shows the progress of a shock wave throughout the material in a highly simplified manner. As the shock wave penetrates into the material, high deviatoric stresses effectively distort the initially cubic lattice into a monoclinic lattice. When these stresses reach a certain threshold level, homogeneous dislocation nucleation can take place. Hirth and Lothe[101] estimate the stress required for homogeneous dislocation nucleation. The nucleation mechanism at the shock front is

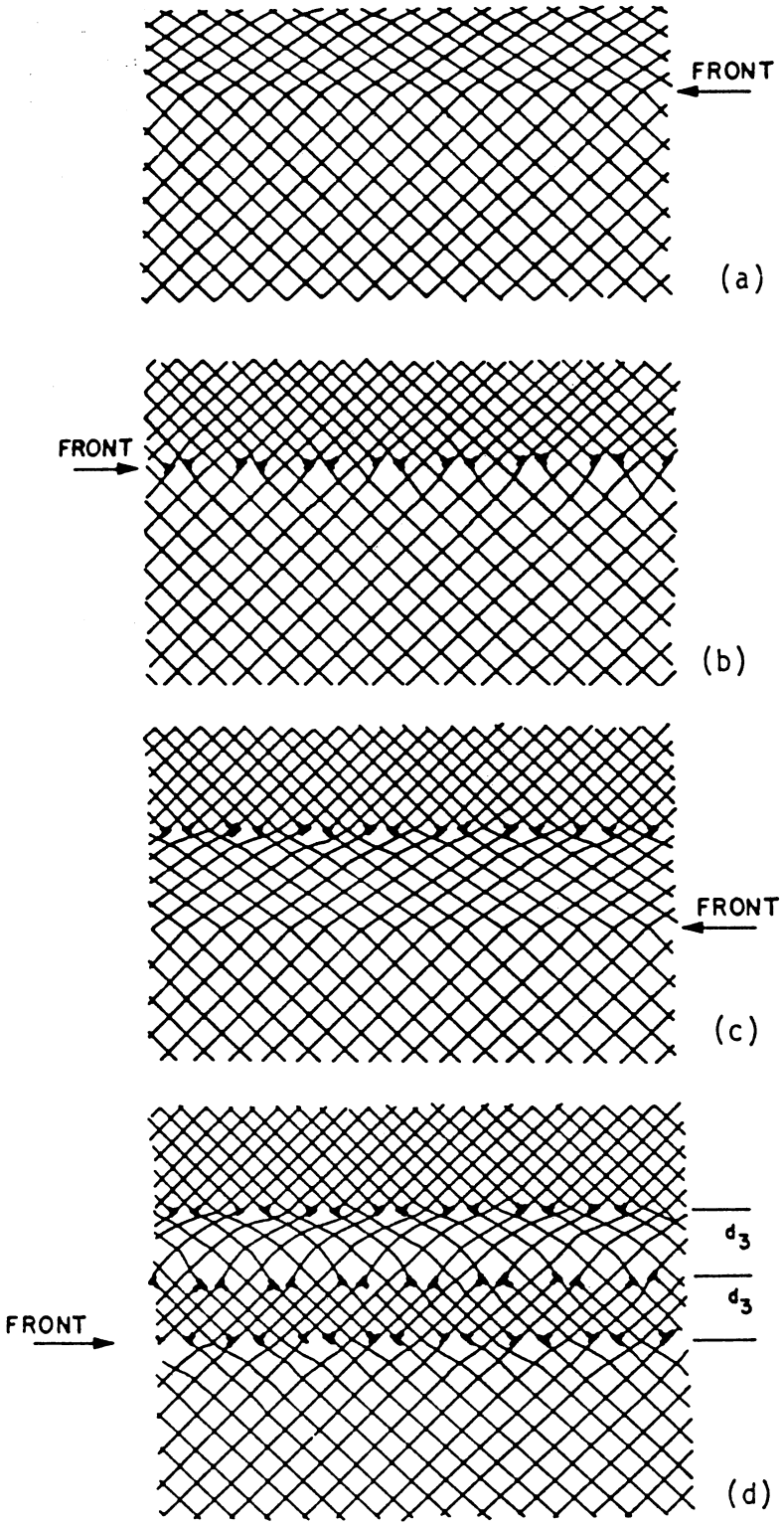

FIG. 2.21 Progress of shock front according to Meyers model.

unique, and different from homogeneous nucleation in conventional deformation. In shock loading, the dislocation interface separates two lattices with different parameters. However, it will be assumed that the stress required is the same, (as a first approximation). From Hirth and Lothe[101] one has:

$$\tau_h/G=0.054 \tag{2.72}$$

where τ_h is the shear stress required and G is the shear modulus, which is pressure-dependent. When the maximum shear stress becomes equal to τ_h (and is acting in the correct orientation), homogeneous dislocation nucleation takes place. Substituting eqn. (2.72) into eqn. (2.68) one obtains:

$$P=0.027\,K$$

This value can be obtained from Fig. 2.8(b) by trial and error. It corresponds to a pressure of approximately 6 GPa. Figure 2.21(b) shows the wave as the front coincides with the first dislocation interface. The density of dislocations at the interface depends on the difference in specific volume between the two lattices and can be calculated therefrom. In Fig. 2.21(c) the front has moved ahead of the interface and the deviatoric stresses build up again; other layers are formed in Fig. 2.21(d). It should be noticed that since the macroscopic strain is ideally zero after the passage of the wave, the sum of the Burgers vectors of all dislocations has to be zero. This is accomplished, in the simplified model presented here, by assuming that adjacent dislocation layers are made of dislocations with opposite Burgers vectors. Figure 2.22 shows two adjacent layers under the effect of shear stresses still existing in the lattice after the dislocations were nucleated; a group of dislocations move away from it. It is possible to estimate the velocity at which these dislocations move if one knows τ_{res}. As these dislocations move, they locally accommodate and decrease τ_{res}. The total amount of internal friction and heat generation due to dislocation motion can be calculated by knowing the difference between the measured and the thermodynamically-calculated residual temperature. A simplified calculation is presented by Hsu *et al*,[68] Greater details of the model as well as comparisons of calculations with measured dislocation densities are presented elsewhere.[71,100]

Recent experimental results[68,102] lead the authors to believe that the rarefaction part of the wave plays only a minor role in dislocation generation. The main reason for this is that the rarefaction part of the wave enters into a material that is already highly dislocated. It was found

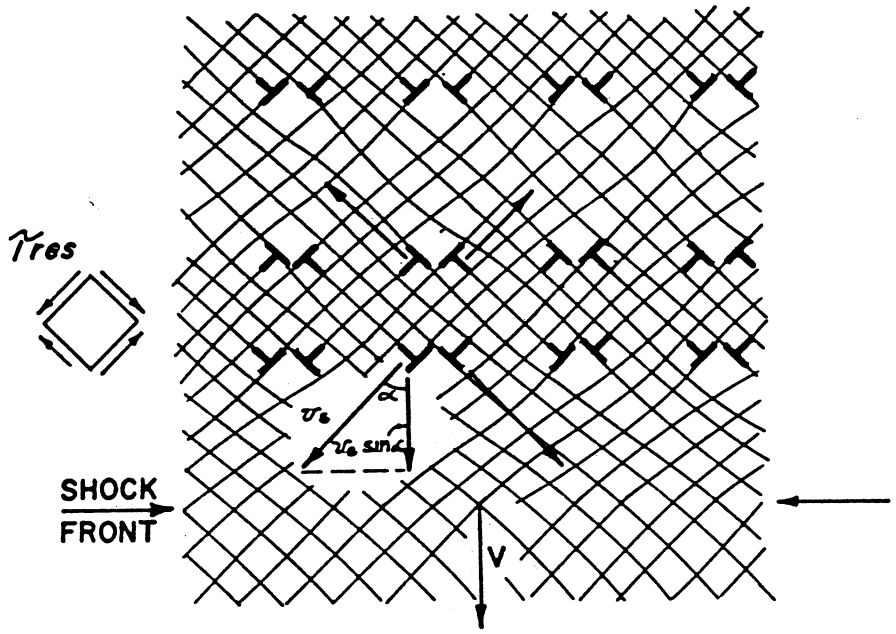

FIG. 2.22 Movement of dislocation generated at the shock front (from ref. 55).

that when nickel is shock-loaded repeatedly, the increase in dislocation density is much less pronounced for the succeeding events.[68,102] The shock wave passing through a highly dislocated material is not such an effective dislocation generator. This is consistent with Meyers' predictions[100] ... 'that if a pre-strained material is shock-loaded, part of the deviatoric stresses at the shock front could be accommodated by existing dislocations; in this case the number of dislocations that would be generated at the front would be reduced. The same argument can be extended to the rarefaction portion of the wave; it can accommodate the deviatoric stresses by the movement of the existing dislocations. Additionally, the time interval in which attenuation takes place is much higher than in which the shock front rises; 200 ns versus 1 ns'.

By using a different approach, Mogilevsky[103,104] independently reached some conclusions similar to those presented here. Computer calculations using a Born–Meyer potential for the atoms allowed Mogilevsky to follow the position of atoms with time. Although a perfect lattice of copper remained elastic up to pressures of 30 GPa, the introduction of point defects allowed the deviatoric stresses to be relaxed by stacking-fault (and, possibly, dislocation) generation at pressures as low as 5 GPa.

An alternative model for dislocations at the shock front was recently

proposed by Weertman.[105] For a strong shock, pulse, he concluded that the front is composed of supersonic and trailing subsonic dislocations. For weaker shock pulses no supersonic interface would be required; arrays of subsonic dislocations, trailing the front (similar to Meyers' dislocations) would attenuate the deviatoric stresses.

2.5.2. Point Defects

Shock loading is also responsible for a high density of point defects. The dynamic strain induced is represented by:

$$\varepsilon_s = \frac{4}{3} \ln\left(\frac{V}{V_0}\right)$$

This corresponds to the sum of the strains imparted by the shock front and the rarefaction part of the wave. In the first systematic comparison between point defects generated by shock loading and cold rolling, Kressel and Brown[70] reported vacancy and interstitial concentrations three to four times higher after shock loading than after cold rolling. However, direct quantitative evidence of vacancies and vacancy-type defects was obtained for the first time by Murr *et al.*[107] Figure 2.23 shows some of the vacancy loops in shock-loaded molybdenum and nickel.[107] Field-ion microscopy showed that these loops in molybdenum accounted for only a small portion of the shock-induced vacancies; the majority exist as single vacancies or small clusters difficult to resolve by conventional electron microscopy.

It is relatively simple to understand why shock loading induces a large concentration of point defects. The primary source of point defects is the non-conservative motion of jogs. These jogs are generated by the intersection of screw or mixed dislocations. Figure 2.22 shows the direction of motion of dislocations under the effect of the residual shear stresses. As they move, τ_{res} decreases, but in the process the dislocations intersect each other, generating jogs. The non-conservative motion of these jogs produces strings of either vacancies or interstitials. These can also occur as dislocation loops when observed in the electron microscope as shown in Fig. 2.23. The subject is treated in detail by Hirth and Lothe.[101] Meyers and Murr[55] describe the model based on non-conservative motion of jogs in detail. For a pressure of 20 GPa in nickel, they find a point-defect concentration of 7×10^{-5}. This compares favorably with results reported by Kressel and Brown,[70] and Graham[108] presents an excellent overview of shock induced point defects.

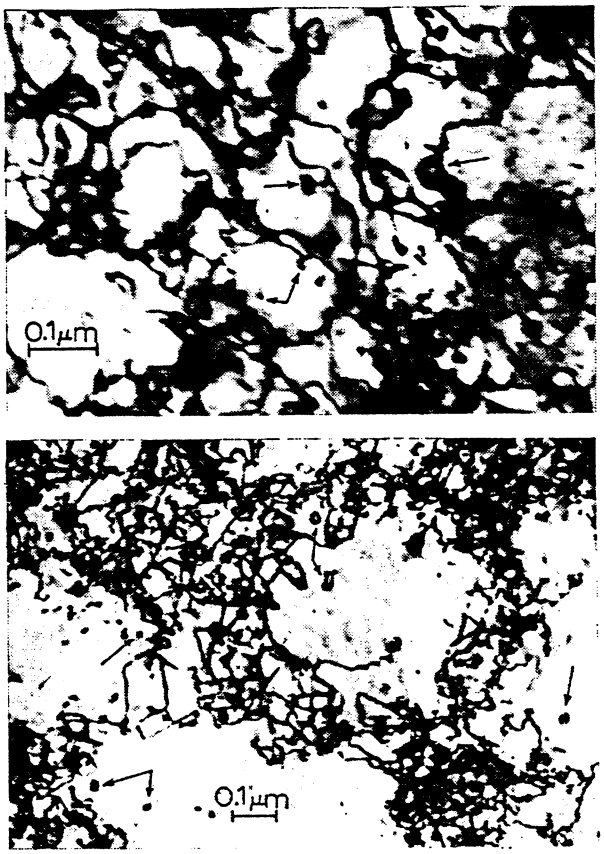

FIG. 2.23 Vacancy-type dislocation loops (arrows) in shock-loaded metals (a) molybdenum shock loaded at 14 GPa, 2 μs; (b) nickel shock loaded at 20 GPa.

2.5.3. Deformation Twinning

The most important and self-consistent comment that can be made about deformation twins is that twinning is a highly favored deformation mode under shock loading. Metals that do not twin by conventional deformation at ambient temperature can be made to twin by shock loading. In this respect, as in the morphology of dislocation substructures, shock deformation resembles conventional deformation at low temperature: loose cell walls and a greater tendency towards twinning. The ease of twinning depends on several factors:

(a) *Pressure*—Nolder and Thomas[109,110] found that twinning occurred, in nickel, above 35 GPa pressure. This was generally confirmed by Greulich and Murr.[111] DeAngelis and Cohen[112] found the same effect in copper.

(b) *Crystallographic orientation*—it is the deviatoric component of

stress that induces twinning. Hence, when the resolved shear stress in the twinning plane and along the twinning direction reaches a critical level, twinning should occur. DeAngelis and Cohen[112] found an orientation dependence for the threshold stress; copper single crystals twinned at 14 GPa when the shock wave traveled along [100] and at 20 GPa when it travelled along [111]. Greulich and Murr[111] found, for nickel, that at and above about 35 GPa, twinning occurred preferentially for [100] grains (Fig. 2.19). As the pressure was increased, the preponderance of twins increased along orientations other than [100].

(c) *Stacking-fault energy*—as the SFE of FCC metals is decreased, the incidence of twinning increases. As a corollary, the threshold stress for twinning should decrease.

(d) *Pulse duration*—the effect of pulse duration, first explored by Appleton and Waddington,[93] was systematically investigated by Champion and Rohde[113] for an austenitic (Hadfield) steel. They found striking differences in twin densities for different pulse durations, at 10 GPa. Numerous twins were observed at 2 μs, while no twinning was present at 0.065 μs. They concluded that there must be a threshold time for twinning. Staudhammer and Murr[114] investigated the effect of pulse duration (0.5, 1, 2, 6, 14 μs) on the substructure of AISI 304 stainless steel. They found an increase in twin density up to about 2 μs; beyond that the twin density seemed to be essentially constant. Stone *et al.*[115] found an increase in twin density as the pulse duration was increased from 0.5 to 1.0 μs, in both the AISI 1008 steel and Armco magnetic ingot iron. The twins generated by the shock pulse should not be confused with the ones formed by the elastic precursor wave, in iron; the latter ones were investigated by Rohde.[116] Although twins are generated by the elastic precursor waves, the volume percent of twins generated by the shock wave is an order of magnitude higher. While the elastic precursor may produce a twin density of 3 vol pct, a shock wave of 30 GPa peak pressure and 1 μs pulse duration has been shown to generate about 50 vol pct of twins.

(e) *Existing substructure*—Rohde *et al.*[117] found profuse twinning upon shock loading titanium-gettered iron in the annealed condition. However, predeformed samples exhibiting a reasonable density of dislocations did not twin. The same results were obtained by Mahajan[118] for iron. Hence, if one looks at dislocation generation and motion, and twinning as competing mechanisms, one can rationalize this response. The deviatoric stresses generated by a shock wave are accommo-

dated by twinning when no dislocations are available and by motion of the already existing dislocations, if iron is predeformed.

(f) *Grain size*—Wongwiwat and Murr[119] were able to explain conflicting data reported in the literature[107,120] on the incidence of twinning in molybdenum by showing that, at a certain pressure, large-grain sized specimens twinned more readily than small-grain sized ones. However, it should be emphasized that this response is not unique to shock loading; indeed, iron–3 pct silicon[121] and chromium[122] have been shown to exhibit a strong grain-size dependence of the twinning stress (in conventional deformation). Kestenbach and Meyers[106,123] investigated the effect of grain size on the substructure of AISI 304 stainless steel.

Two fundamentally different mechanisms have been proposed to account for twin formation. The first involves a pole mechanism proposed by Cottrell and Bilby[124] for BCC metals, and extended to FCC metals by Venables.[125] The pole mechanism involves dislocation motion which sweeps out the twin spiraling around a dislocation pole. This requires a rather longer time than generally available in shock loading, and this velocity or time limitation led Cohen and Weertman[126] to propose a much simpler model, especially applicable to FCC metals and alloys. This latter model involves the production and systematic glide motion of Shockley partial dislocations on every [111] plane to produce a twin which propagated with the velocity of propagation of the partial dislocation. Sleeswyk[127] has also proposed a model for twin formation in BCC metals which is phenomenologically identical to that of Cohen and Weertman[126] in FCC materials. Sleeswyk's model involves the systematic glide of dislocations on [112] planes in the BCC structure.

2.5.4. Displacive/Diffusionless Transformations

There are numerous instances in which a shock wave induces a phase transformation. A very detailed review is presented by Graham and Duvall;[128] for this reason, only a classification scheme will be presented here. The phase transformations involving diffusion are excluded from this discussion. Stein[129] has shown that precipitation is induced by shock loading.

Cohen *et al.*[130] recently proposed a classification scheme for displacive/diffusionless transformations. The first division is between shuffle and lattice-distortive transformations; the latter group is divided into two sub-groups; dilatation-dominant and deviatoric-dominant transformations. The term martensitic (and quasi-martensitic) is reserved for the lattice distortive transformations in which the deviatoric

component of stress is dominant. Hence only the FCC→BCC (or BCT) and FCC→HCP transformation in the Fe-base alloys and the BCC→ close packed transformations in the noble metal alloys can be called martensitic. A whole range of phase transformations, such as the beta–omega in Ti alloys and the tetragonal–cubic transformation in tin, cannot be called martensitic.

The effect of a shock pulse on a displacive/diffusionless transformation has to be analysed from three points of view: (a) pressure; (b) shear stresses and (c) temperature. The changes in these parameters are not independent; there are specific temperature rises and deviatoric stresses associated with a certain pressure level. Nevertheless, they have different effects on the thermodynamics of phase transformation. A phase transformation resulting in a reduction of volume, for example is thermodynamically favored at high pressure, because it will tend to decrease the pressure in that region. On the other hand, a phase transformation in which the product has a lower density is not favored by the pressure. Figure 2.24 shows the pressure–temperature diagram for iron. At a certain critical pressure, the BCC (α) phase transforms to either HCP (ε) or FCC (γ), depending upon the temperature. Both these phases are more closely packed than α(BCC). Figure 2.24 also shows that the pressure increase is coupled to a temperature increase. Hence, the pressure path

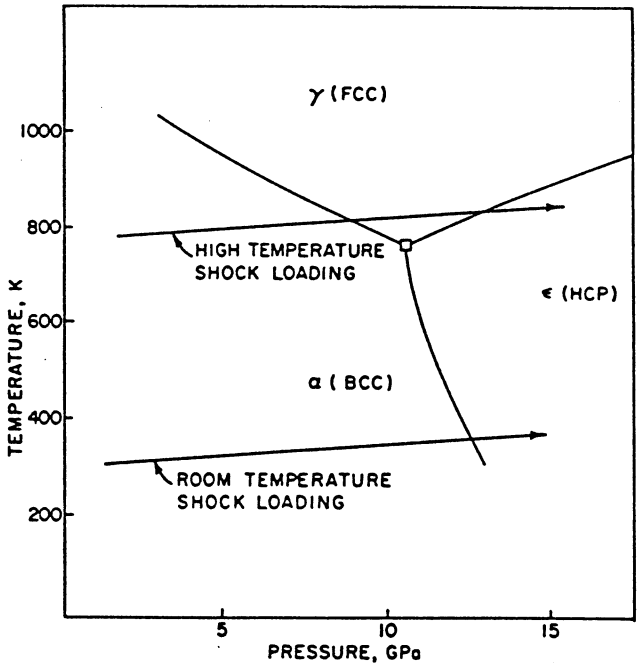

FIG. 2.24 Temperature–pressure diagram for iron.

has a slight slope. Plutonium is another metal that is very interesting from a metallurgical point of view. It undergoes six different phase transformations, some with large differences in density.[131] The room temperature monoclinic phase has a high density (19.86); hence the pressure will not induce phase transformation. On the other hand, if the shock wave passes through one of the lower density phases, it will favor its transformation into the higher-density phases. Plutonium is unique in that melting is accompanied by a volume decrease. Hence, the pressure has the effect of reducing the melting point; in metals where the melting point is associated with an expansion, pressure increases the melting point. Some of the transformations in Pu alloys are, due to the large density changes, considered as dilatation-dominant, and are therefore not considered as martensitic. Patel and Cohen[132] have established a rationale for the effect of stresses on the M_s temperature in martensite transformations. They found that, in Fe-30 pct Ni alloy, the hydrostatic pressure decreased the M_s temperature. In these alloys, there is a dilatation of 5 pct associated with the martensitic phase. Hence, a pressure pulse should not favor the transformation, and this is reflected in the decrease in M_s. On the other hand, an alloy in the martensitic form should revert to austenite, if a pressure pulse were applied, because this would result in a contraction of the lattice.[123] A negative pressure pulse inducing negative hydrostatic pressures would be the converse situation and the γ(FCC)$\rightarrow\alpha$(BCC or BCT) transformation would be favored, with an increase in the transition temperature. Meyers and Guimarães[134] were able to produce a tensile pulse and generate martensite in an Fe-31 pct Ni–0.1 pct alloy. Figure 2.25 shows the martensite tube generated by tensile waves; this tensile wave was produced by a compressive shock wave, as it reflected at a free surface. The region of the material traversed by the compressive wave exhibited only a dense array of dislocations organized in cells and occasional twins. This phenomenon was used to calculate a nucleation time for the martensitic transformation.[135]

The effect of shear stresses always associated with the pressure is more difficult to assess. In deviatoric-dominant transformations the externally applied shear stresses can play an important role in the initiation of transformation. The transformation is favored along the crystallographic orientations in which the transformation shear will tend to decrease the externally-applied shear, and will tend to decrease the overall internal energy. Martensite can be considered as a deformation mechanism competing with slip and twinning, and externally applied shear stresses

FIG. 2.25 Martensite generated by tensile hydrostatic stresses produced by a reflected pressure pulse in an iron–nickel alloy (from ref. 134). Bar = 100 μm.

increase M_s. The shear stresses introduced by the shock waves tend to favor the generation of martensite. However, these shear stresses are much lower than the hydrostatic stresses for most shock waves, because dislocation nucleation and twinning will attenuate them. Hence, they will only generate martensite when the temperature at the shock front is slightly higher than M_s. In this case martensite transformation can effectively compete with twinning and slip. Olson and Cohen[136] have shown that, during conventional deformation at temperatures slightly above M_s, yielding is produced by stress-induced martensite. The same phenomenon was confirmed by Guimarães *et al.*[137] Up to 20 K above M_s, yielding was initiated by martensitic transformation. Hence, one can conclude that the shear stresses associated with shock loading might be important in martensite nucleation if the temperature at the shock front is within 50 K of the M_s under the imposed conditions (at the level of pressure established by the shock pulse). These features are demonstrated by Staudhammer *et al.*,[138] who also show that martensite forms exclusively in 304 stainless steel at the intersections of twin-faults by a strain-induced process described previously.[136] This process involves the selective movement and interaction of groups of partial dislocations, at temperatures well above the M_s temperature for the stainless steel (which is below 4 K). When Shockley partial dislocations of the type $\alpha/6\langle 112\rangle$ are created on every other $\{111\}$ plane, a packet of HCP (ε) martensite is created. When these bundles intersect with more complex faulting arrays (such as $3a/8\langle 112\rangle$ fault arrays), α' (BCC) martensite is created within the intersection volume. Once nucleated, strain-induced intersection martensite (α) can grow by coalescence of the intersection volumes, or by stress-assisted processes. In other words, once formed, martensite growth can be somewhat catastrophic when a stress assist is imposed. For example, having created some martensite by an initial shock pulse, a subsequent shock may induce considerably more martensite. In addition, shock pressure applied in longer pulses at high pressure can have a similar effect.[89]

2.5.5. Other Effects

There are a number of other shock effects which are mentioned only briefly in concluding this section. These relate mainly to the impedance differences encountered by the shock wave which can manifest themselves in velocity differences, etc. The realization of the anisotropy of elastic and plastic properties of the individual grains in a polycrystalline material led to a 'wavy-mode' model which attempted to account for

such differences.[139] However, at higher pressures ($P \gtrsim 10$ GPa) velocity differences due to crystallographic orientations are practically imperceptible, and in general the shock wave is not significantly affected.

Wave reflection and refraction at grain boundaries and other internal asperities which arise by difference in structure and composition can also occur by impedance discontinuities. These effects are, however, also of secondary importance at high pressures (>10 GPa). None the less, second-phase particles can play a significant role in the generation of defects, particularly dislocations. This feature is especially prominent at coherent precipitates which lack coherence with the shock wave passage, and the loss of coherence is accommodated by the creation of dislocations which can also multiply. Das and Radcliffe[140] have observed the punching out of dislocations at precipitates and such phenomena can also lead to nucleation of other defects, such as twins as illustrated by Leslie *et al.*[141]

ACKNOWLEDGEMENTS

The writing of this chapter was conducted while one of us (M.A.M.) was supported by the Research and Development Division of New Mexico Tech. The help of Dr. M. Brook in making this support available is greatly acknowledged. Appreciation is extended to Professor G. Purcell, Chairman of the Department of Metallurgical and Materials Engineering, for provision of facilities.

REFERENCES

1. KOLSKY, H. *Stress Waves on Solids*, Dover, New York, 1963.
2. RINEHART, J. S. *Stress Transients in Solids*, Hyperdynamics, Santa Fe, New Mexico, P.O. Box 392, 1975.
3. GHATAK, A. K., and KOTHARI, L. S. *An Introduction to Lattice Dynamics*, Addison-Wesley, Reading, Mass., 1972, p. 70.
4. LEE, E. H. In *Shock Waves and the Mechanical Properties of Solids*, eds. J. J. Burke and V. Weiss, Syracuse U. Press, Syracuse, 1971, p. 3.
5. VON KÁRMÁN, T., and DUWEZ, P. *J. Appl. Phys.*, 21 (1950), 987.
6. CLIFTON, R. J. Source cited in ref. 4, p. 73.
7. HERRMANN, W. In *Propagation of Shock Waves in Solids*, ed. E. Varley, ASME, AMD-17, New York, 1976, p. 1.
8. CHOU, P. C. In *Dynamic Response of Materials to Intense Impulsive Loading*, eds. P. C. Chou and A. K. Hopkins, Air Force Materials Laboratory, WPAFB, 1972, p. 55.

9. HERRMANN, W., and NUNZIATO, J. W. Source cited in ref. 8, p. 123.
10. WASLEY, R. J. *Stress Wave Propagation in Solids*, M. Dekker, New York, 1973.
11. RICE, M. H., MCQUEEN, R. G., and WALSH, J. M. *Solid State Physics*, 6, (1958), 1.
12. DAVISON, L., and GRAHAM, R. A. *Phys. Rep.*, 55 (1979), 257.
13. BRADLEY, J. N. *Shock Waves in Chemistry and Physics*, J. Wiley, New York, 1962.
14. KINSLOW, R., ed. *High-Velocity Impact Phenomena*, Academic, New York, 1970.
15. ZELDOVICH, Ya. B., and RAIZER, Yu. P. *Physics of Shock Waves and High-Temperature Hydrodynamic Phenomena*, Academic, New York, 1966.
16. WILKINS, M. In *Methods in Computational Physics*, Vol. 3, eds. B. Alder, S. Fernbach, and M. Rotenberg, Academic, New York, 1964, p. 211.
17. HERRMANN, W., HICKS, D. L., and YOUNG, E. G. Source cited in ref. 4, p. 23.
18. WALSH, R. T. Source cited in ref. 8, p. 363.
19. KARPP, R., and CHOU, P. C. Source cited in ref. 8, p. 283.
20. ROHDE, R. W., BUTCHER, B. M., HOLLAND, J. R., and KARNES, C. H. *Metallurgical Effects at High Strain Rates*, Plenum, New York, 1973.
21. MEYERS, M. A., and MURR, L. E., eds. *Shock Waves and High-Strain-Rate Phenomena in Metals: Concepts and Applications*, Plenum, New York, 1981.
22. KREYZIG, E. *Advanced Engineering Mathematics*, 2nd ed., Wiley, 1971, pp. 490, 512.
23. MEYERS, M. A., and CARVALHO, M. S. *Mat. Sci. Eng.*, **24** (1976), 131.
24. CRITESCU, N. *Dynamic Plasticity*, Interscience Publishers, New York, 1967.
25. ABOU-SAYED, A. S. *Analysis of Combined Pressure-Shear Waves in an Elastic/Visco-Plastic Material*, M.Sc. Thesis, Brown U., 1972.
26. ABOU-SAYED, A. S. *Analytical and Experimental Investigation of Pressure-Shear Waves in Solids*, Ph.D. Thesis, Brown U., 1975.
27. ABOU-SAYED, A. S., CLIFTON, R. J., and HERMANN, L. *Exptl. Mech.*, (1976) 127.
28. GRAHAM, R. A., and ASAY, J. R. *High Temp–High Press.*, **10** (1978), 355.
29. DECARLI, P. S., and MEYERS, M. A. Source cited in ref. 21, p. 341.
30. ORAVA, R. N., and WITTMAN, R. H. *Proc. 5th Intl. Conf. High Energy Rate Fabrication*, U. of Denver, Colorado, 1975, P. 1.1.1.
31. EZRA, A. A. ed., *Principles and Practice of Explosive Metalworking*, Industrial Newspapers Ltd., London, 1973.
32. TAYLOR, G. I. *J. Inst. Civil Engrs.*, **26** (1946), 486.
33. RAKHMATULIN, K. A. *Appl. Math. and Mech.*, **9** (1945), No. 1.
34. POCHAMMER, L. *J. reine angew. Math.*, **81** (1876), 324.
35. CHREE, C. *Trans. Camb. Phil. Soc.*, **14** (1889), 250.
36. TING, T. C. T., and NAN, N. *Trans. ASME, J. Appl. Mech.*, 36, (1969), 189.
37. BLEICH, H. H., and NELSON, I. *Trans. ASME, J. Appl. Mech.*, 33, (1966), 149.
38. LEE, E. H. *J. Appl. Mech.* 36 (1969), 1.
39. CLIFTON, R. J. Plastic waves: theory and experiment, in *Mechanics Today*, ed. S. Nemat-Nasser, Vol. 1, Pergamon Press, 1972.

40. HIRTH, J. P. *Met Trans.*, **9A** (1978), 401.
41. National Materials Advisory Board Report NMAB-356, 1980, National Academy of Sciences, 1980.
42. HOPKINSON, B. *Roy. Soc. Phil. Trans.*, **A213** (1914), 437.
43. DAVIES, R. M. *Roy. Soc. Phil. Trans.*, **A240** (1948), 375.
44. KOLSKY, H. *Proc. Roy. Soc. London*, **62B** (1949), 676.
45. RANKINE, W. J. M. *Phil. Trans. Roy. Soc., London*, **160** (1870), 270.
46. HUGONIOT, H. J. *J. L'Ecole Polytechnique*, **58** (1889), 3.
47. RICE, M. H., MCQUEEN, R. J. and WALSH, J. M. Compression of Solids by Strong Shock Waves, in *Solid State Physics*, Vol. 6, p. 1, Academic Press, New York (1958).
48. VAN THIEL, M. *Compendium of Shock Wave Data*, UCRL-50108, Lawrence Radiation Laboratory, Univ. of California, 1966.
49. MCQUEEN, R. J. Source cited in ref. 14, p. 293.
50. MCQUEEN, R. J. and MARSH, S. P. *J.A.P.*, **31**, (1960), 1253.
51. DUVALL, G. E. Source cited in ref. 8, p. 481.
52. MCQUEEN, R. J., MARSH, S. P., TAYLOR, J. W., FRITZ, J. N. Source cited in ref. 14, p. 293.
53. MEYERS, M. A. *Thermomechanical Processing of a Nickel-Base Superalloy by Cold Rolling and Shock-Wave Deformation*, Ph.D. Thesis, U. of Denver, Colorado, 1974.
54. DUVALL, G. E., and GRAHAM, R. A. *Rev. Modern Phys.*, **49** (1977), 523.
55. MEYERS, M. A., and MURR, L. E. Source cited in ref. 21, p. 487.
56. VON NEUMANN, J., and RICHTMYER, R. D. *J. Appl. Phys.*, **21** (1950), 2322.
57. DRUMMOND, W. E. *J. Appl. Phys.*, **29** (1958), 167.
58. BERTHOLF, L. D., and BENZLEY, S. E. *TOODY II, A Computer Program for Two-Dimensional Wave Propagation*, Sandia Laboratories Research Laboratory SC–RR–68–41 (1968).
59. LAWRENCE, R. J. *WONDY III – A Computer Program for One-Dimensional Wave Propagation*, Sandia Laboratories Development Report SC–DR–70–715 (1970).
60. DIENES, J. K., and WALSH, J. M. Source cited in ref. 14, p. 45.
61. CURRAN, D. R., SEAMAN, L., and SHOCKEY, D. A. *Physics Today*, Jan., 1977, 46.
62. SEAMAN, L., TOKHEIM, R., and CURRAN, D. *Computational Representation of Constitutive Relations for Porous Material*, S.R.I. Report DNA 3412F, May 1974.
63. HOENIG, C., HOLT, A., FINGER, M., and KUHL, W. *Proc. 5th Intl. Conf. High Energy Rate Fabrication*, U. of Denver, Colorado, June 1974, p. 6.3.1.
64. CURRAN, D. R. *J.A.P.*, **34**, 2677.
65. ERKMAN, J. O., CHRISTENSEN, A. B., and FOWLES, G. R. *Attenuation of Shock Waves in Solids*, Technical Report No. AFWL–TR–66–72, Stanford Research Institute, Air Force Weapons Laboratory, May, 1966.
66. REMPEL, J. R., SCHMIDT, D. N., ERKMAN, J. O., and ISBELL, W. M. *Shock Attenuation in Solid and Distended Materials*, Standford Research Institute, Technical Report No. WL–TR–65–119, Air Force Weapons Laboratory, February, 1966.
67. ERKMAN, J. O., and CHRISTENSEN, A. B. *J.A.P.*, **38** (1967) 5395.

68. HSU, C. Y., HSU, K. C., MURR, L. E. and MEYERS, M. A. Source cited in ref. 21, p. 433.
69. DIETER, G. E. *Mechanical Metallurgy*, 2nd ed., McGraw-Hill (1976), p. 169.
70. KRESSEL, H., and BROWN, N. J. *J. Appl. Phys.*, **38** (1967), 1618.
71. MEYERS, M. A. In *Strength of Metals and Alloys*, Vol. I., eds. P. Haasen, V. Gerold, and G. Kostorz, Pergamon Press, New York, (1979), p. 549.
72. TAYLOR, J. W., and RICE, M. H. *J. Appl. Phys.* **34** (1963), 364.
73. TAYLOR, J. W. *J. Appl. Phys.* **36** (1965), 3146.
74. JOHNSON, W. G., and GILMAN, J. J. *J. Appl. Phys.*, **30** (1959), 129.
75. BARKER, L. M., BUTCHER, B. M., and KARNES, C. H. *J. Appl. Phys.*, **37** (1966), 1989.
76. HOLLAND, J. R. *Acta Met.*, **15** (1967), 691.
77. KELLY, J. M., and GILLIS, P. P. *J. Appl. Phys.*, **38** (1967), 4044.
78. CONRAD, H., and WIEDERSCH, H. *Acta Met.* **8** (1960), 128.
79. JOHNSON, J. N. *J. Appl. Phys.*, **40** (1969), 2287.
80. ROHDE, R. W. *Acta Met.*, **17** (1969), 353.
81. MEYERS, M. A. *Mat. Sci. Eng.*, **30** (1977), 99.
82. JONES, O. E., and HOLLAND, J. R. *Acta Met.* **16** (1968), 1037.
83. ZENER, C., and HOLLOMON, J. H. *J. Appl. Phys.*, **15** (1944), 22.
84. RECHT, R. F. *J. Appl. Mech.*, **31** (1964), 189.
85. CULVER, R. S. Source cited in ref. 20, p. 519.
86. ROGERS, H. C. *Ann. Rev. Mater. Sci.*, **9** (1979), 283.
87. OLSON, G. B., MESCALL, J. F., and AZRIN, M. Source cited in ref. 21, p. 221.
88. YELLUP, J. M., and WOODWARD, R. L. *Res Mechanica*, **1** (1980), 41.
89. MEYERS, M. A. *Mater. Sci. Eng.*, **51** (1981), 261.
90. MURR, L. E., and KUHLMANN-WILSDORF, D. *Acta Met.*, **26** (1978), 849.
91. MEYERS, M. A. *Met. Trans.*, **8A** (1977), 1641.
92. MURR, L. E. Source cited in ref. 21, p. 753.
93. APPLETON, A. S., and WADDINGTON, J. S. *Acta Met.*, **12** (1963), 681.
94. MARSH, E. T., and MIKKOLA, D. E. *Scripta Met.*, **10** (1976), 851.
95. MEYERS, M. A., KESTENBACH, H-J., and SOARES, C.A.O. *Mat Sci. Eng.*, **45** (1980), 143.
96. KOUL, M. K., and BREEDIS, J. F. In *The Science, Technology, and Application of Titanium*, eds. R. I. Jaffee and N. E. Promisel, Pergamon, Oxford, 1978, p. 817.
97. MURR, L. E., and GALBRAITH, J. *J. Mtls. Sci.*, **10** (1975), 2025.
98. SMITH, C. S. *Trans. AIME*, **212** (1958), 574.
99. HORNBOGEN, E. *Acta Met.*, **10** (1962), 978.
100. MEYERS, M. A. *Scripta Met.*, **12** (1978), 21.
101. HIRTH, J. P. and LOTHE, J. *The Theory of Dislocations*, McGraw-Hill, New York, (1968), p. 689.
102. KAZMI, B., and MURR. L. E. Source cited in ref. 21, p. 733.
103. MOGILEVSKY, M. A. *Proc. Symp. on High Dynamic Pressure*, Paris, August (1978).
104. MOGILEVSKY Source cited in ref. 21, p. 531.
105. WEERTMAN, J. Source cited in ref. 21, p. 469.
106. MEYERS, M. A. *Proc. ICM II*, Boston, Mass., August 16–20, 1976, p. 1804.

107. MURR, L. E. INAL, O. T., and MORALES, A. A. *Appl. Phys. Letters*, **28** (1976), 432.
108. GRAHAM, R. A. Source cited in ref. 21, p. 375.
109. NOLDER, R. L., and THOMAS, G. *Acta Met.*, **11** (1963), 994.
110. NOLDER, R. L., and THOMAS, G. *Acta Met.*, **12** (1964), 227.
111. GREULICH, F., and MURR, L. E. *Mater. Sci. Engr.*, **39** (1978), 81.
112. DEANGELIS, R. J., and DOHEN, J. P. *J. Metals*, **15** (1963), 681.
113. CHAMPION, A. R. and ROHDE, R. W. *J. Appl Phys.*, **41** (1970), 2213.
114. MURR, L. E., and STAUDHAMMER, K. P. *Mater. Sci. Engr.*, **20** (1974), 95.
115. STONE, G. A., ORAVA, R. H., GRAY, G. T., and PELTON, A. R. *An Investigation of the Influence of Shock-Wave Profile on the Mechanical and Thermal Responses of Polycrystalline Iron*, Final Technical Report, U.S. Army Research Office, Grant No. DAA629-76-0181, p. 30, 1978.
116. ROHDE, R. W. *Acta Met.*, **17** (1969), 353.
117. ROHDE, R. W., LESLIE, W. C., and GLENN, R. C. *Met. Trans.*, **3A** (1972), 363.
118. MAHAJAN, S. *Phys. Stat. Sol.*, **33a** (1969), 291.
119. WONGWIWAT, K., and MURR, L. E. *Mater. Sci. Engr.*, **35** (1978), 273.
120. VERBRAAK, C. A. *Science and Technology of W, Ta, Mo, Nb, and Their Alloys*, Pergamon Press, N.Y., 1964, p. 219.
121. MARCINKOWSKI, M. J., and LIPSITT, H. A. *Acta Met.*, **10** (1962), 951.
122. HALL, D. *Acta Met.*, **9** (1961), 191.
123. KESTENBACH, H-J., and MEYERS, M. A. *Met. Trans.*, **7A** (1976), 1943.
124. COTTRELL, A. H., and BILBY, J. *Phil. Mag.*, **42** (1951), 573.
125. VENABLES, J. A. *Phil. Mag.*, **6** (1961), 379.
126. COHEN, J. B., and WEERTMAN, J. *Acta Met.*, **11** (1963), 997.
127. SLEESWYK, A. W. *Acta Met.*, **10** (1962), 803.
128. DUVALL, G. E., and GRAHAM, R. A. *Reviews of Modern Physics*, **49** (1977), 523.
129. STEIN, C. *Scripta Met.*, **9** (1975), 67.
130. COHEN, M., OLSON, G. B., and CLAPP, P. C. *Proceedings ICOMAT 1979*, MIT Press, Cambridge, Mass. 1980, p. 1.
131. HECKER, S. S. Private communication, Los Alamos National Laboratory (1981).
132. PATEL, J. R., and COHEN, M. *Acta Met.*, **1** (1953), 531.
133. ROHDE, R. W., HOLLAND, J. R. and GRAHAM, R. A. *Trans. Met. Soc. AIME*, **242** (1968), 2017.
134. MEYERS, M. A., and GUIMARÃES, J. R. C. *Mater. Sci. Engr.*, **24** (1976), 289.
135. MEYERS, M. A. *Met. Trans.*, **10A** (1979), 1723.
136. OLSON, G. B., and COHEN, M. *J. Less Common Metals*, **28** (1972), 107.
137. GUIMARÃES, J. R. C., GOMES, J. C., and MEYERS, M. A. *Suppl. to Trans. J.I.M.*, 1976 (1741).
138. STAUDHAMMER, K. P., FRANTZ, C. E., HECKER, S. S., and MURR, L. E. Source cited in ref. 21, p. 91.
139. MEYERS, M. A. *Mater. Sci. Engr.*, **30** (1977), 99.
140. DAS, G., and RADCLIFFE, S. V. *Phil. Mag.*, **20** (1969), 589.
141. LESLIE, W. C., STEVENS, D. W., and COHEN, M. In *High-Strength*

Materials, V. F. Zackay (ed.), John Wiley and Sons, New York, 1965, p. 382.
142. EDINGTON, J. W. *Phil. Mag.*, **19** (1969), 1189.
143. EDINGTON, J. W. In *Mechanical Behavior of Materials Under Dynamic Loads*, ed. U.S. Lindholm, Springer, Berlin, 1968, 191.
144. NYE, J. F. *Physical Properties of Crystals*, Oxford U. Press, London, 1959.